Bulletin of the Seismological Society of America, Vol. 95, No. 6, pp. 2373–2395, December 2005, doi: 10.1785/0120040128

Hysteretic and Dilatant Behavior of Cohesionless Soils and Their Effects on Nonlinear Site Response: Field Data Observations and Modeling

by Luis Fabián Bonilla, Ralph J. Archuleta, and Daniel Lavallée

Abstract In this study we present evidence that nonlinearity can be directly observed in acceleration time histories such as those recorded at the Wildlife Refuge and Kushiro Port downhole arrays from the 1987 Superstition Hills, California, and the 1993 Kushiro-Oki, Japan, earthquakes, respectively. These accelerograms and others compiled in this study present a characteristic waveform composed of intermittent high-frequency peaks riding on a low-frequency carrier. In addition, soil amplification of the surface records is strongly observed compared to their downhole counterpart; this is contrary to the expected amplification reduction produced by the nonlinear soil behavior. Laboratory studies show that the physical mechanism that produces such phenomena is the dilatant nature of cohesionless soils, which introduces the partial recovery of the shear strength under cyclic loads. This recovery translates into the ability to produce large deformations followed by large and spiky shear stresses. The spikes observed in the acceleration records are directly related to these periods of dilatancy and generation of pore pressure. These results are significant in strong-motion seismology because these spikes produce large if not the largest acceleration. They are site related, not source related.

Using the *in situ* observations from the Kushiro Port downhole array, we have modeled the 1993 Kushiro-Oki earthquake. The synthetic accelerograms show the development of intermittent behavior—high frequency peaks—as observed in the recorded acceleration time histories. Shear modulus degradation due to pore pressure produces large strains in the soil with large amplification in the low-frequency band of the ground motion. We also modeled data from the 1987 Superstition Hills earthquake recorded at the Wildlife Refuge station. The results show the importance of better soil characterization when pore pressure may develop and the effects of dilatancy in the understanding of nonlinear site response.

Introduction

Nonlinear site response studies have been around for the last 35 years within the engineering community. The evidence of nonlinear soil behavior comes from experimental cyclic tests on soil samples where it is an observed departure from the linear state as well as hysteresis when large strains are produced (e.g., Hardin and Drnevich, 1972a,b; Vucetic, 1990). Several attempts to model complete nonlinear site response have been done in the past (e.g., Joyner and Chen, 1975; Lee and Finn, 1978; Pyke, 1979), and few others have worked on the effects expected on an earthquake record when traveling in a nonlinear medium (Yu *et al.*, 1992; Ni *et al.*, 1997; Hartzell *et al.*, 2004).

Seismologists generally model ground motion using a linear site response even at strong-motion levels. The basis for such modeling can be seen, for instance, in the use of empirical Green's functions, which have proven to be effective in modeling strong ground motion (e.g., Hartzell, 1978; Hutchings, 1991). Amplification factors derived from weak and strong motion are similar (Aki, 1993). In addition, seismologists question the degree of nonlinearity and its importance for assessing strong ground motion because some nonlinear effects can be masked by other phenomena such as signal noise and uncertainties in soil parameters, among others (Field *et al.*, 1997; O'Connell, 1999).

Most of the studies about soil nonlinearity vary from simple state equations with a few parameters (e.g., Hardin and Drnevich, 1972a,b; Pyke, 1979; Prevost and Keane, 1990) to complex formulations with dozens of parameters (e.g., Zienkiewicz *et al.*, 1982; Prevost and Popescu, 1996; Ramsamooj and Alwash, 1997). These equations represent the stress-strain relation, the so-called backbone curve, whose parameters are calibrated with laboratory data. Naturally the more complete and complex the model, the more expensive becomes its characterization. Indeed, one reason

why the equivalent linear model (Schnabel *et al.*, 1972) is often used is that it needs few parameters. Consequently, its computation is stable and relatively fast compared to any fully nonlinear time domain method (Kausel and Assimaki, 2002).

The incorporation of hysteresis in the stress-strain relation of any fully nonlinear analysis is fundamental. Although the equivalent linear method may produce similar results for site response studies in some particular cases, that method is stress-strain path independent. Thus, the modulus reduction and damping factors represent only particular states in the strain-stress space and not the whole stress-strain evolution. The model that is commonly used to simulate hysteresis in soils is the one proposed by Masing (1926). In this model the stress-strain paths are computed by scaling and shifting their current position with respect to the last reversal by a factor of two. Iwan (1967) proposed a method that describes the hysteresis of a nonlinear material by a series of springs connected either in series or parallel. His method follows exactly the Masing criteria. Another approach is to describe such hysteretic behavior through a set of rules. Such rules provide a phenomenological description of the soil hysteresis; they describe the evolution of the stress-strain path at any time. The evolution of the stress-strain path is based on laboratory results. This set of rules is known as the Masing rules (Vucetic, 1990; Kramer, 1996).

While nonlinearity in seismic ground motion is often inferred, there are only few cases where nonlinearity has been directly observed in strong ground motion accelerograms. Moreover, predicting strong ground motion time histories requires quantifying the degree of nonlinearity associated with different levels of input motion coupled with characteristics of the site geology (Hartzell *et al.*, 2004). In this study we present a new characteristic of accelerograms that we believe is a direct result of nonlinearity in the soil during strong ground shaking. To understand the soil nonlinear behavior we combine a general hysteresis formulation (Bonilla, 2000) and pore pressure generation following stress-strain constitutive models of Towhata and Ishihara (1985) and Iai *et al.* (1990a,b). These models are implemented in a nonlinear one-dimensional finite-difference code. We use this formulation to examine two case histories of known nonlinear soil response as well as to investigate the role of critical parameters in affecting the soil behavior.

Nonlinearity in Observed Accelerograms

Among the clearest examples of nonlinear response are the Port Island borehole records of the 1995 Hyogo-ken Nanbu (Kobe) earthquake (Iwasaki and Tai, 1996). In the acceleration records there is a clear change in the high-frequency waveforms of acceleration with less obvious changes in the low-frequency velocity and displacement time histories. While not as direct an observation as from borehole recordings, nonlinear response is generally associated with accelerograms that show a pronounced change in frequency content that occurs during or immediately after strong shaking. A classic example of such behavior is the response at Treasure Island (a soft soil site) during the 1989 Loma Prieta earthquake. Fortunately there was an accelerogram recorded on rock about two kilometers away at Yerba Buena Island for comparison (Fig. 1).

Other than borehole observations of strong shaking or in the serendipity situation where accelerograms are recorded at rock and soil sites close to each other, nonlinearity of the soil must be inferred by indirect methods. A basic approach is to compare the transfer function for weak and strong ground motion recorded at the same site (for a review of seismological observations see Beresnev and Wen, 1996). The principal observation one expects for nonlinear response is a shift of the fundamental frequency of the transfer function to longer period (e.g., Idriss and Seed, 1968). A major difficulty with this approach is finding a reference site. Using data from the 1994 Northridge earthquake Field *et al.* (1997) compared the average amplification of strong and weak shaking for a class of soil sites with that of a few rock sites to infer widespread nonlinear soil response at frequencies between 1.0 and 4.0 Hz. O'Connell (1999) has shown that linear response and scattering of waves in the upper kilometers of the earth's crust can explain much of the same data used by Field *et al.* (1997). In a study of the 1989 Loma Prieta earthquake, Idriss (1990) compared peak accelerations on rock sites compared to soil sites for the same event to infer nonlinear response. Borehole data provide an excellent baseline for such studies (Satoh *et al.*, 1995, 1997; Wen *et al.*, 1994). However the downgoing waves (those reflected from the free surface and other pronounced changes in impedance) can produce suspicious peaks in the transfer function that might be interpreted as a shift in the fundamental frequency (Steidl *et al.*, 1996).

Characteristic Waveform

In some strong motion accelerograms Archuleta (1998) observed that there is a characteristic waveform associated with nonlinear response of soils. One of the most obvious examples of this waveform is clearly observed in the Port Kushiro surface acceleration time history (Fig. 2) resulting from the 1993 Kushiro-Oki earthquake (Iai *et al.*, 1995). Thorough analysis of this surface record by Iai *et al.* (1995) leaves no doubt that the spiky waveform is the result of nonlinear response of the soil. Porcella (1980) had described such waveforms as being *atypical accelerograms.* Porcella wrote, "It is hoped that future recordings from these stations will contain some indication of the origin and nature of these high-frequency, large amplitude spikes." Porcella cited as examples of atypical accelerograms: Bonds Corner, 15 October 1979 Imperial Valley earthquake (Fig. 3); Cerro Prieto accelerogram, 9 June 1980 northern Mexico earthquake; and four recordings at the left abutment of Long Valley Dam from four $M > 6$ earthquakes in May 1980 near Mammoth Lakes.

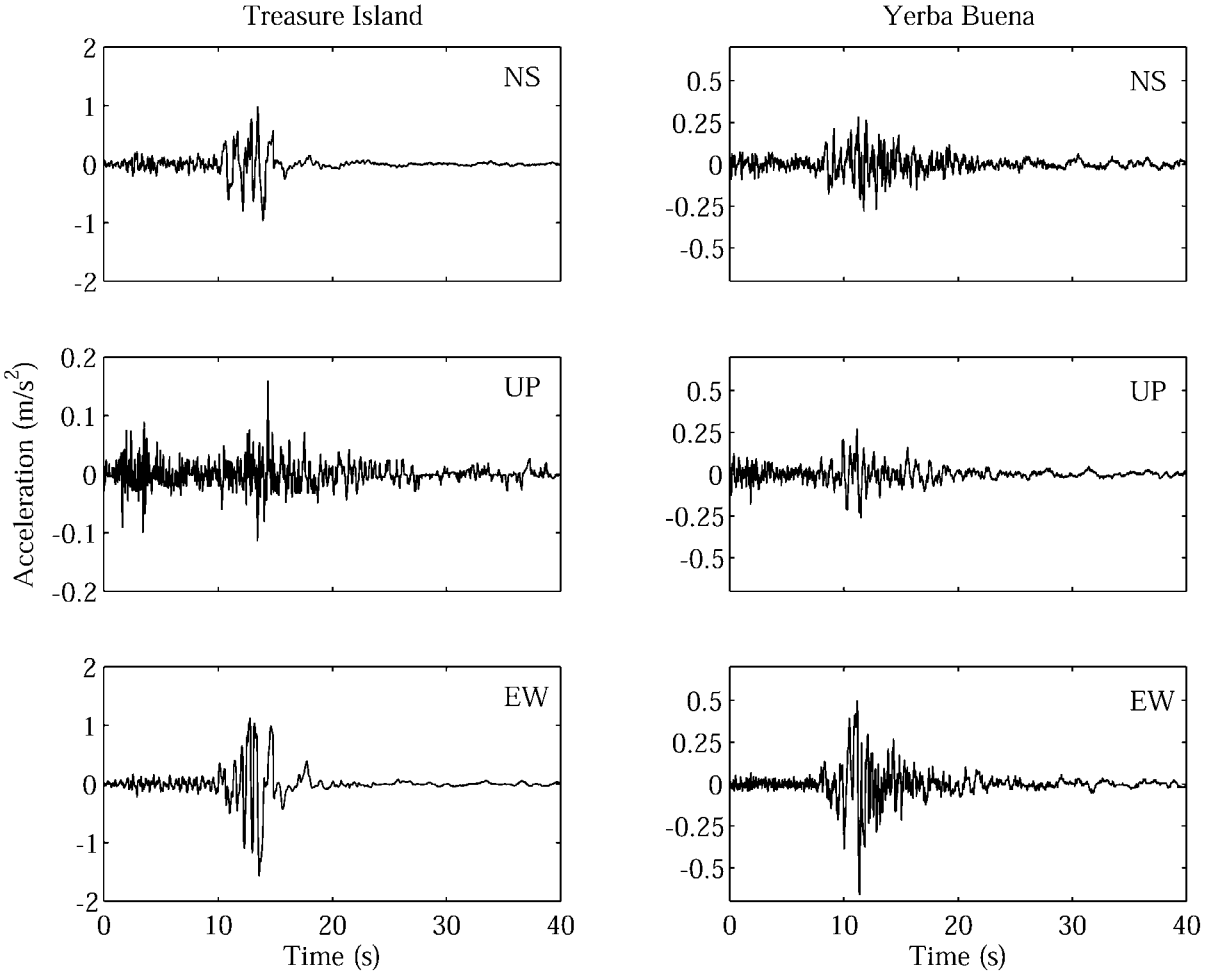

Figure 1. Accelerograms from the 1989 Loma Prieta earthquake recorded at Treasure Island (soil) and Yerba Buena (rock) stations. These two sites are within 2.5 km of each other.

This characteristic waveform is also present in the Wildlife Refuge recordings of the 1987 Superstition Hills earthquake (Holzer *et al.*, 1989; Zeghal and Elgamal, 1994), (Fig. 4); the fault normal Takatori accelerogram of the 1995 Hyogo-ken Nanbu (Kobe) earthquake (Kamae *et al.*, 1998), (Fig. 5); the 1994 Northridge accelerograms recorded at Jansen Main Building (JMB) and Sylmar Converter Station (SCS) in the Van Norman Dam Complex (Bardet and Davis, 1996), (Fig. 6). In Figure 6 we also show a rock recording of Los Angeles Dam located 1.2 km from these two records. Finally, the 2001 Nisqually accelerograms recorded at stations SDS, SDW, and HAR (Frankel *et al.*, 2002) also show this peculiar waveform (Fig. 7).

This characteristic waveform is a direct consequence of nonlinear soil response as shown by the analysis at Kushiro Port (Iai *et al.*, 1995) and the Wildlife Refuge (Zeghal and Elgamal, 1994). In the analysis of the records at the Wildlife Refuge array, Zeghal and Elgamal (1994) associated the spikes in the acceleration time histories with episodes of dilatancy in the corresponding pore pressure measurements that were simultaneously recorded (Holzer *et al.*, 1989). The Wildlife Refuge site experienced liquefaction at the surface; but the Kushiro Port site did not.

This manifestation of nonlinearity, multiple occurrences of similar shaped acceleration spikes, is significantly different from previous observations where nonlinear effects diminish the high frequency nature of accelerograms reducing the peak acceleration. In the case of Kushiro-Oki (Fig. 2), Bonds Corner (Fig. 3), Supersition Hills (Fig. 4), Sylmar Converter Station (Fig. 6), and SDS station from the Nisqually earthquake (Fig. 7), the maximum acceleration is a peak associated with one of these characteristic waveforms. The other critical effect is that the nonlinearity extends the duration of strong shaking as opposed to the commonly held view that nonlinearity reduces the duration of strong shaking, for example, Treasure Island (Fig. 1). This nonlinear effect creates a time history that has, late in the record, high acceleration pulses that are a site effect, not a source effect.

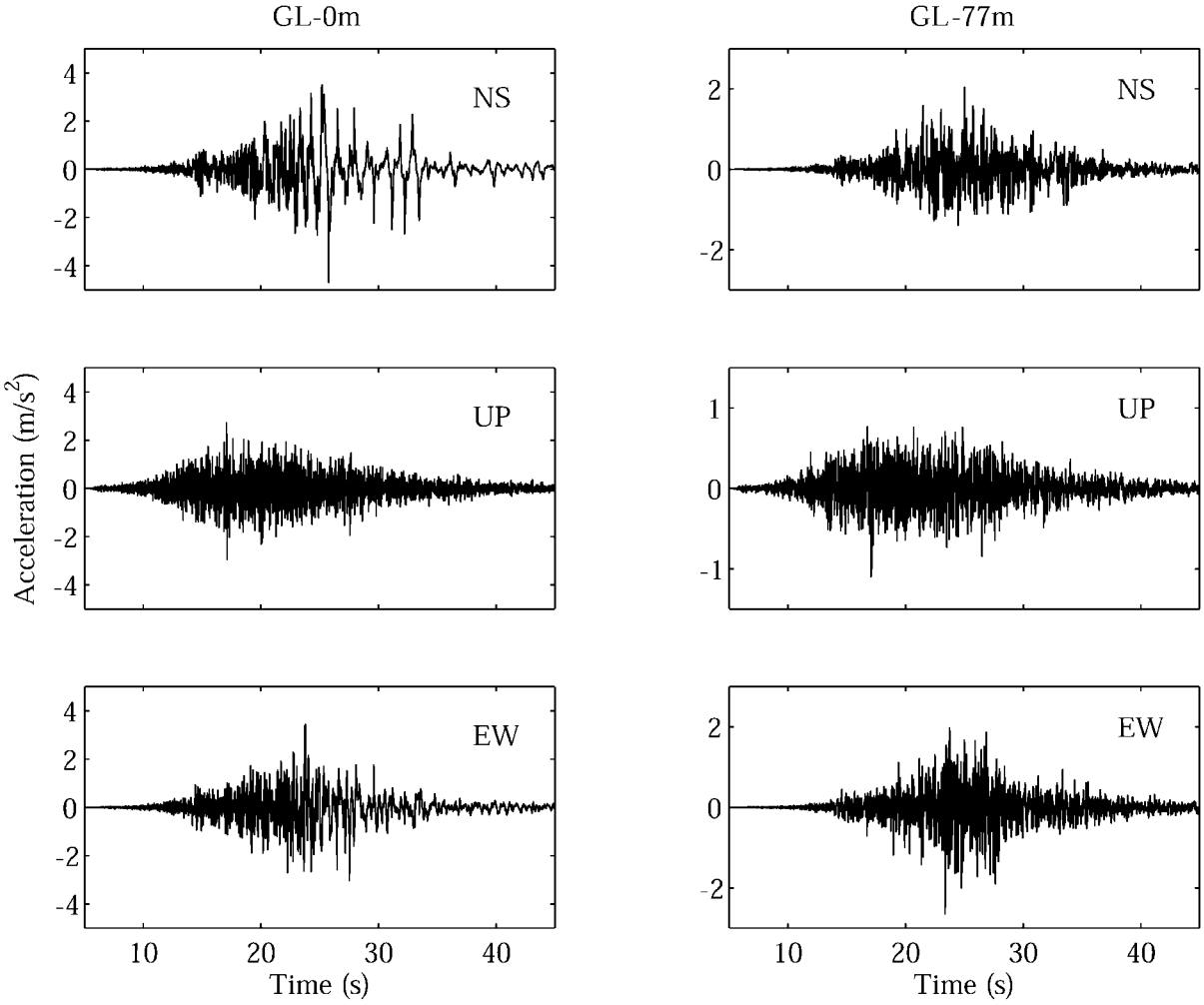

Figure 2. Surface (GL-0 m) and borehole (GL-77 m) acceleration time histories for a dense sand deposit during the 1993 Kushiro-oki earthquake. Note the spiky repetitive waveform that dominates the surface starting at about 25 sec.

Constitutive Model of Soil: The Strain Space Multishear Mechanism Model

The propagation of seismic waves directly depends on the material properties of the medium through which they travel. To understand the phenomenology of nonlinear soil response to earthquakes, we need models that capture the essential physics of soil nonlinearity such as hysteretic behavior and pore pressure generation.

The multishear mechanism model (Towhata and Ishihara, 1995) is a plane strain formulation to simulate pore pressure generation in sands under cyclic loading and undrained conditions. Iai *et al.* (1990a,b) modified the model to account for the cyclic mobility and dilatancy of sands. This method has the following strong points:

- It is relatively easy to implement. It has few parameters that can be obtained from simple laboratory tests that include pore pressure generation.
- This model represents the effect of rotation of principal stresses during cyclic behavior of anisotropically consolidated sands.
- Since the theory is a plane strain condition, it can be used to study problems in two dimensions, for example, embankments, quay walls, among others.

In two-dimensional cartesian coordinates and using vectorial notation, the effective stress σ' and strain ε tensors can be written as

$$\{\sigma'\}^T = \{\sigma'_x \ \sigma'_y \ \tau_{xy}\}$$
$$\{\varepsilon\}^T = \varepsilon_x \ \varepsilon_y \ \gamma_{xy}\},$$

where the superscript T represents the vector transpose operation; σ_x, σ_y, ε_x, and ε_y represent the normal stresses and strains in the horizontal and vertical directions; τ_{xy} and γ_{xy} are the shear stress and shear strain, respectively.

The multiple mechanism model relates the stress and strain through the following incremental equation (Iai *et al.*, 1990a,b),

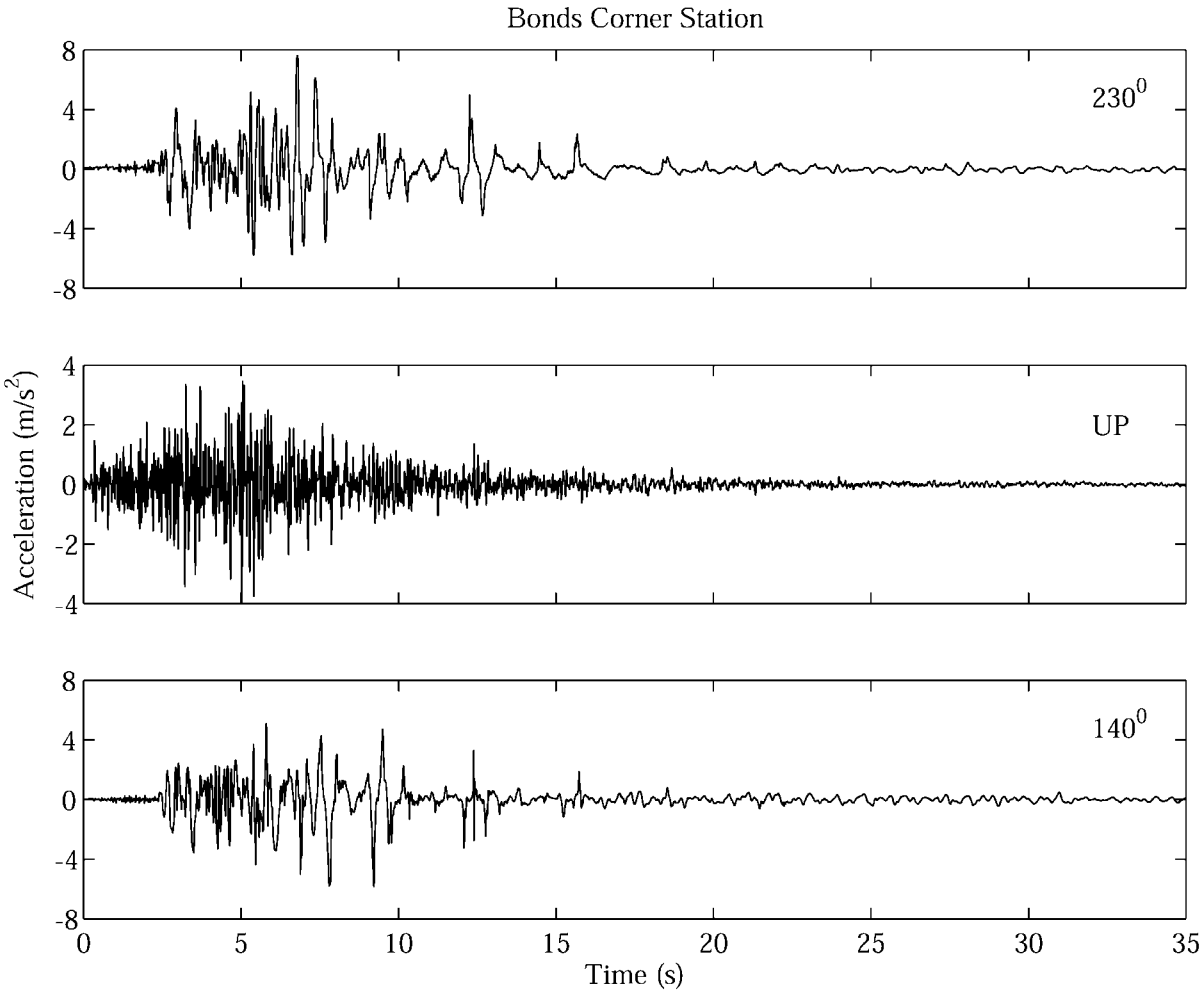

Figure 3. Accelerograms recorded at Bonds Corner station during the 1979 Imperial Valley earthquake. Note the spiky acceleration starting around 6 sec and coming after the main *S* waves.

$$\{d\sigma'\} = [D](\{d\varepsilon\} - \{d\varepsilon_p\}),$$

where the curly brackets represent the vector notation; $\{\varepsilon_p\}$ is the volumetric strain produced by the pore pressure, and $[D]$ is the tangential stiffness matrix given by

$$[D] = Kn^{(0)}n^{(0)T} + \sum_{i=1}^{I} R^{(i)}n^{(i)}n^{(i)T}.$$

The first term is the volumetric mechanism represented by the bulk modulus K. The second part is the shear mechanism represented by the tangential shear modulus $R^{(i)}$ idealized as a collection of I springs (Fig. 8). Each spring follows the hyperbolic stress-strain model (Konder and Zelasko, 1963) during the loading and unloading hysteresis process. The shear mechanism may also be considered as a combination of pure shear and shear by differential compression. In addition,

$$\begin{aligned} n^{(0)T} &= \{1\ 1\ 0\} \\ n^{(i)T} &= \{\cos\theta_i - \cos\theta_i \sin\theta_i\} \\ \theta_i &= (i-1)\,\Delta\theta \\ \Delta\theta &= \pi/I, \end{aligned}$$

where $\Delta\theta$ is the angle between each spring as shown in Figure 8.

Towhata and Ishihara (1985) found, using laboratory data, that the pore pressure excess is correlated with the cumulative shear work produced during cyclic loading. Iai *et al.* (1990a, b) developed a mathematical model that needs five parameters, called hereafter dilatancy parameters, to take into account this correlation. These parameters represent the initial and final phases of dilatancy, p_1 and p_2; overall dilatancy, w_1; threshold limit and ultimate limit of dilatancy, c_1 and S_1. These parameters are obtained by fitting laboratory data, obtained from either undrained stress controlled cyclic shear tests or from cyclic stress ratio curves. Details of this constitutive model can be found in Iai *et al.*

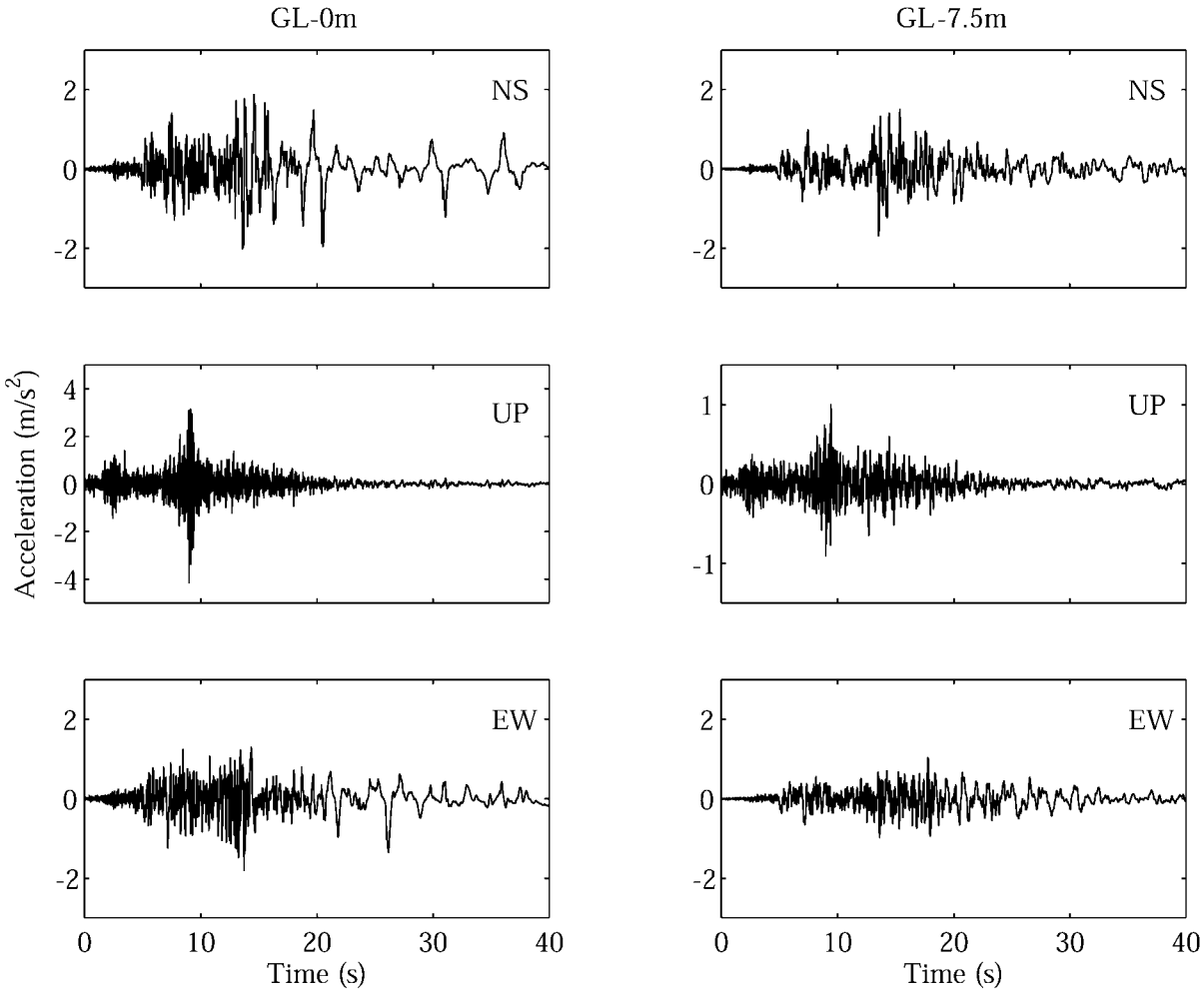

Figure 4. Accelerograms recorded at the Wildlife Refuge vertical array for the M 6.7 Superstition Hills earthquake. Note the spiky waveforms in the acceleration time histories on the horizontal components.

(1990a,b). In addition, the hysteresis model is fully described in Bonilla (2000).

Nonlinearity in Dilatant Saturated Soils

Behavior of Dilatant Soils

At any depth, a soil element is subjected to an initial effective mean pressure σ'_{m0}. In a horizontally layered soil model, there is only the mean pressure acting on the soil element prior to the earthquake. When the seismic waves arrive, the soil element is sheared by the stress, τ_{xy}. This shear stress will induce a change in the mean pressure; the principal stresses in the Mohr's circle will rotate due to the presence of the shear stress. The change in mean pressure is translated into a change of the volumetric strain. This is coupled to the volumetric strain produced by the pore pressure generation. The constitutive equation, which describes the material rheology, determines the volumetric strain change due to shearing. The multiple shear mechanisms simulates this volumetric change. We will see in the oncoming sections the effect of seismic waves into dilatant materials, in particular, cohesionless soils.

Yet, what is a dilatant soil? Ishihara (1996, p. 246) wrote: " . . . a deposit of sand is composed of an assemblage of particles in equilibrium where inter-granular forces are transmitted through points of contact. When shear stress is applied, the resulting deformation is always accompanied by a volume change which is known as dilatancy. This shear-induced volume change accrues as a result of two competing modes of particle movement, namely, slip-down and roll-over . . ." He continues, " . . . the slip-down movement of grains tends to reduce the volume by repacking the sand aggregate into a denser state. This mechanism is activated predominantly in loose deposits of sand. The roll-over mechanism tends to increase the volume which is characteristic in the behavior of dense sand. . . ." However, the most important effect is the following, " . . . when the slip-down takes place, particles are filling gaps in the void and not moving largely in the direction of shearing. Therefore, the

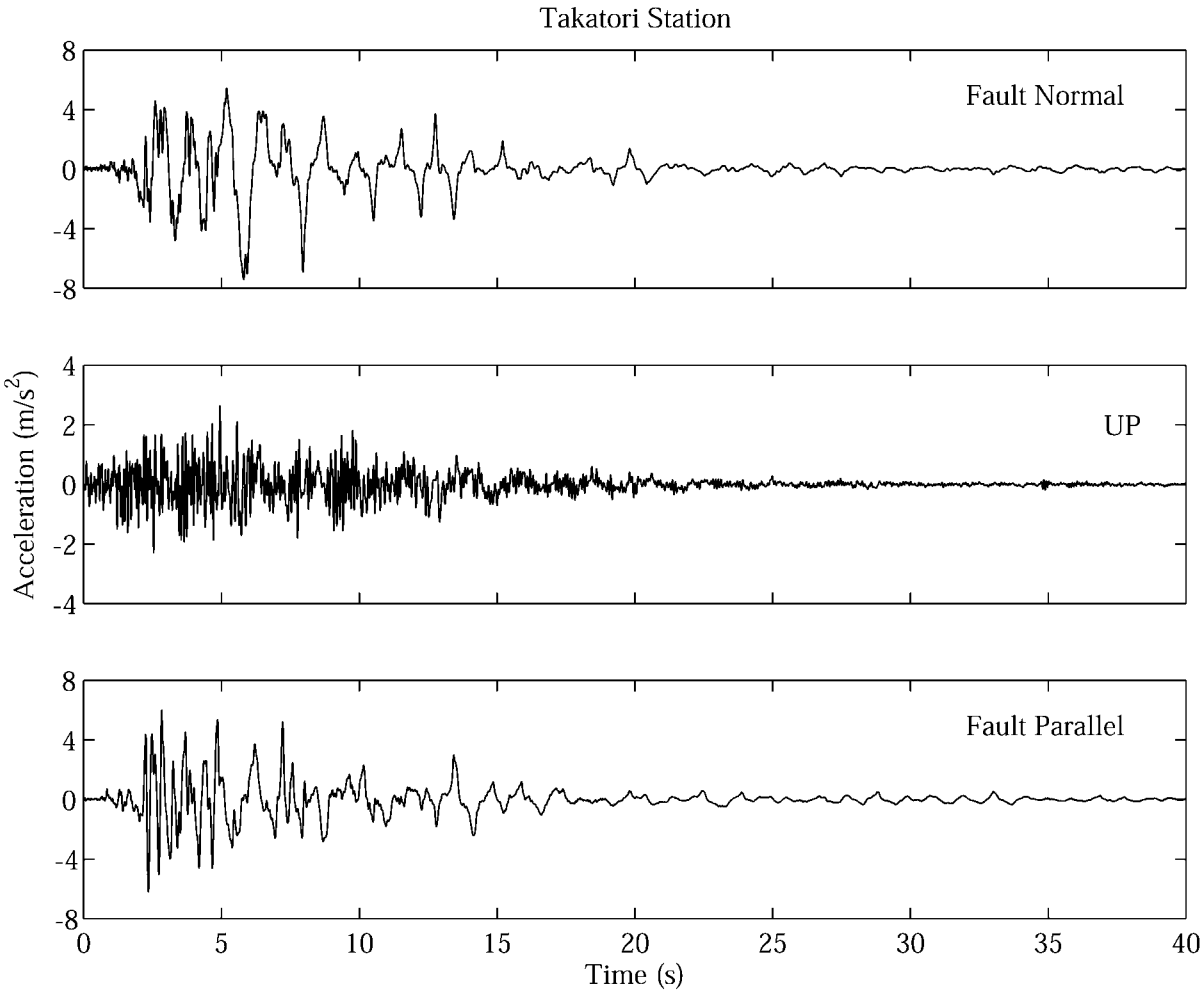

Figure 5. Accelerograms from the 1995 Hyogo-ken Nanbu (Kobe) earthquake recorded at the Takatori station. Observe that the characteristic waveform is predominant on the fault normal component.

slip-down movement can occur rather easily without mobilizing a large amount of shear strain. . . . On the contrary, a larger movement is always required for particles to roll over neighbouring ones and hence the volume increase or dilation is generally induced at a later stage of shear stress application where the sand is largely deformed . . ."

Obviously, both the slip-down and rollover mechanisms occur at the same time. The slip-down mechanism produces a contractive behavior, and the rollover produces a dilatant behavior. The contractive and dilatant zones are fully appreciated in a plot of the shear stress versus the effective mean normal stress (Fig. 9). Such plots, also known as stress path plots, show the reduction of the effective mean stress during shear loading. They are equivalent to a time-dependent Mohr's diagram where $\sigma'_m = \sigma'_{m0}$ at $t = t_0$. The effective mean stress σ'_m is reduced as time increases. The failure line is given by the sine of the angle of internal friction ϕ (Jaeger and Cook, 1979). The transition from contractive to dilative behavior is characterized by the phase transformation angle ϕ_p, where $\phi_p < \phi$ (Ishihara and Towhata, 1982; Iai *et al.*, 1990a). Figure 9 shows a stress path for a simple shear stress controlled experiment on a dense sand. These laboratory data come from the Verification of Liquefaction Analysis with Centrifuge Studies (VELACS Project) (Arulanandan and Scott, 1993). The effective mean stress, σ'_m, and the shear stress, τ_{xy}, are normalized with respect to the initial effective mean stress, σ'_{m0}. Note the contractive behavior (monotonically reduction of the effective mean stress) up to about 0.6. Once the stress path enters into the dilative zone, there is a partial increase of the mean stress and becomes larger as the effective mean stress is reduced.

The Wildlife Refuge Liquefaction Array: Identification of Dilatancy Using Borehole Data

Borehole data are becoming more important nowadays because they not only provide data for direct site response estimation (provided that the downhole recording is in stiff

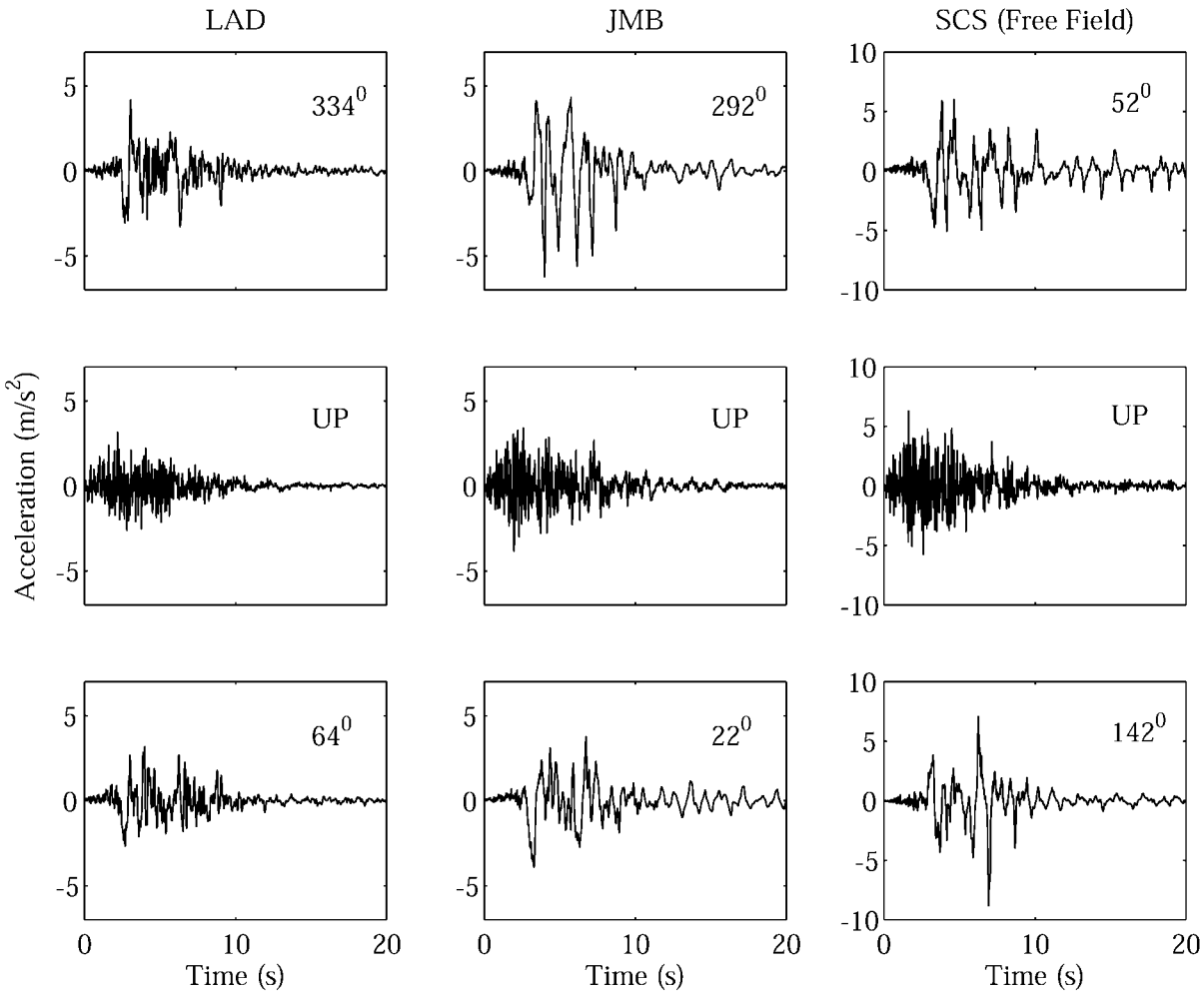

Figure 6. Accelerograms from the 1994 Northridge earthquake recorded at Los Angeles Dam (LAD), Jensen Main Building (JMB), and Sylmar Converter Station (SCS) in the Van Norman Dam Complex in the San Fernando Valley. Stations JMB and SCS are located on soil, and station LAD is located on rock.

material), but also for studying the different levels at which nonlinearity may be present. Indeed, thus far borehole data have been the only direct confirmation of nonlinearity (e.g., Seed and Idriss, 1970; Zeghal and Elgamal, 1994; Beresnev *et al.*, 1995; Iai *et al.*, 1995; Aguirre and Irikura, 1997).

One direct *in situ* observation of nonlinearity in borehole data is from the M_L 6.6 24 November 1987 Superstition Hills earthquake. The Wildlife Refuge liquefaction array recorded acceleration at the surface and 7.5-m depth, and pore pressure on six piezometers at various depths (Holzer *et al.*, 1989). Critically, the array also recorded the M_L 6.2 23 November 1987 Elmore Ranch earthquake that occurred about 12 hours before the Superstition Hills event. The Elmore Ranch earthquake did not produce any pore pressure record.

The acceleration time histories for the Elmore Ranch and Superstition Hills events at GL-0 m and GL-7.5 m, respectively, are shown in Figure 10. Note how the acceleration changes abruptly for the Superstition Hills record at GL-0 m after the *S* wave. Several sharp peaks are observed; they are very close to the peak acceleration for the whole record. In addition, these peaks have lower frequency than the previous part of the record (the beginning of the *S* wave, for instance).

Zeghal and Elgamal (1994) used the Elmore Ranch and the Superstition Hills earthquakes to estimate the stress and strain from borehole acceleration recordings. They approximated the shear stress $\tau_{xy}(y, t)$ at depth y, and the mean shear strain $\bar{\gamma}_{xy}(t)$ between the two sensors,

$$\tau_{xy}(y,t) = \frac{1}{2}\rho y[\ddot{u}(0,t) + \ddot{u}(y,t)]$$

$$\bar{\gamma}_{xy}(t) = \frac{u(h,\,t) - u(0,\,t)}{h},$$

where $\ddot{u}(0,\,t)$ is the horizontal acceleration at the ground surface, $\ddot{u}(y,\,t)$ is the acceleration at depth y (evaluated

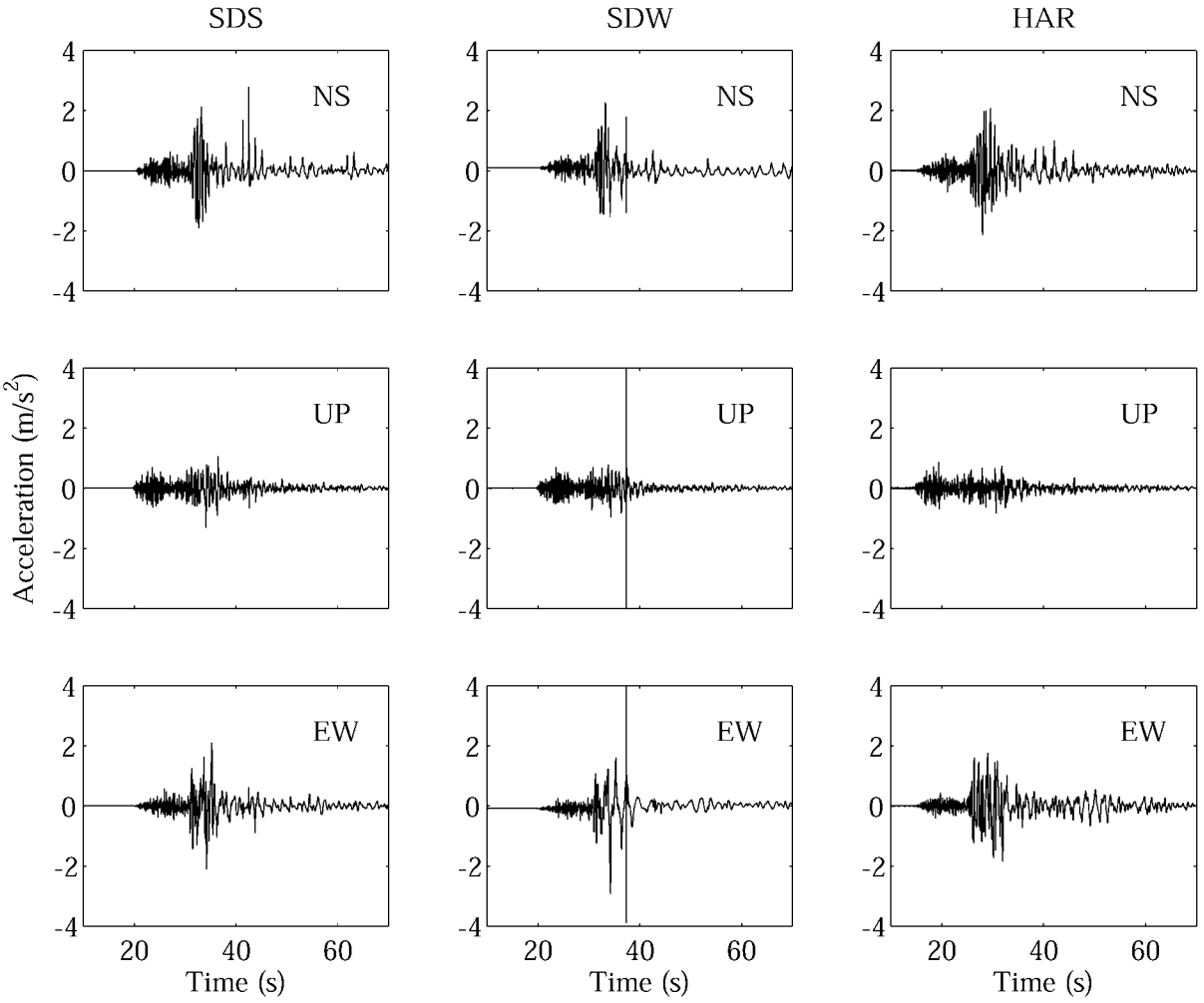

Figure 7. Accelerograms from the 2001 Nisqually earthquake recorded at SDS, SDW, and HAR stations. All stations are located on artificial alluvium with an average shear wave velocity in the first 30 m less than 180 m/sec. The large spike in station SDW probably comes from a falling object (Frankel *et al.*, 2002).

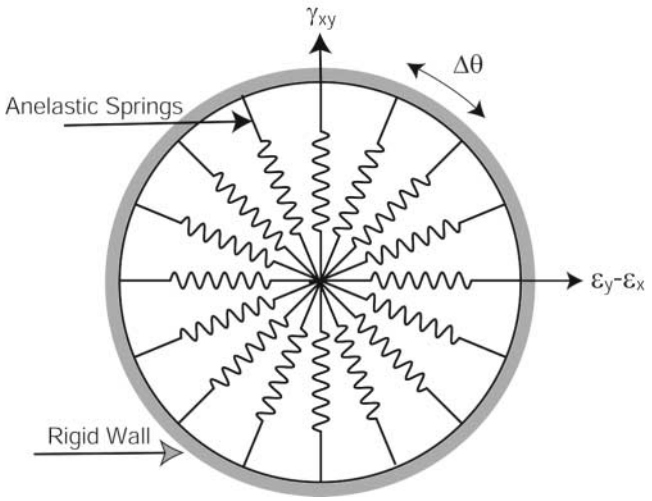

Figure 8. Schematic figure for the multiple simple shear mechanism. The plane strain is the combination of pure shear (vertical axis) and shear by compression (horizontal axis). After Towhata and Ishihara (1985).

through linear interpolation, $\ddot{u}(y, t) = \ddot{u}(0, t) + (\ddot{u}(h, t) - \ddot{u}(0, t))(y/h))$; $\ddot{u}(h, t)$ is the acceleration at the bottom of the layer; $u(h, t)$ and $u(0, t)$ are the displacement histories obtained by integrating twice the corresponding acceleration histories; h is the thickness of the layer; and ρ is the density.

Using this method, the stress and strain at GL-2.9 m were computed (Fig. 11). This figure clearly shows the large nonlinearity developed during the Superstition Hills event. The stress-strain loops form an S shape and the strains are as large as 1.5%. At this depth, there is a piezometer (P5). With this information it is possible to reconstruct the stress path (Fig. 12). Note that some of the pore pressure pulses are correlated with episodes of high shear stress development. The stress path shows a strong contractive phase followed by dilatancy when the effective mean stress is close to 15 kPa. The failure and transformation lines are also plotted using values suggested by Zeghal *et al.* (1996).

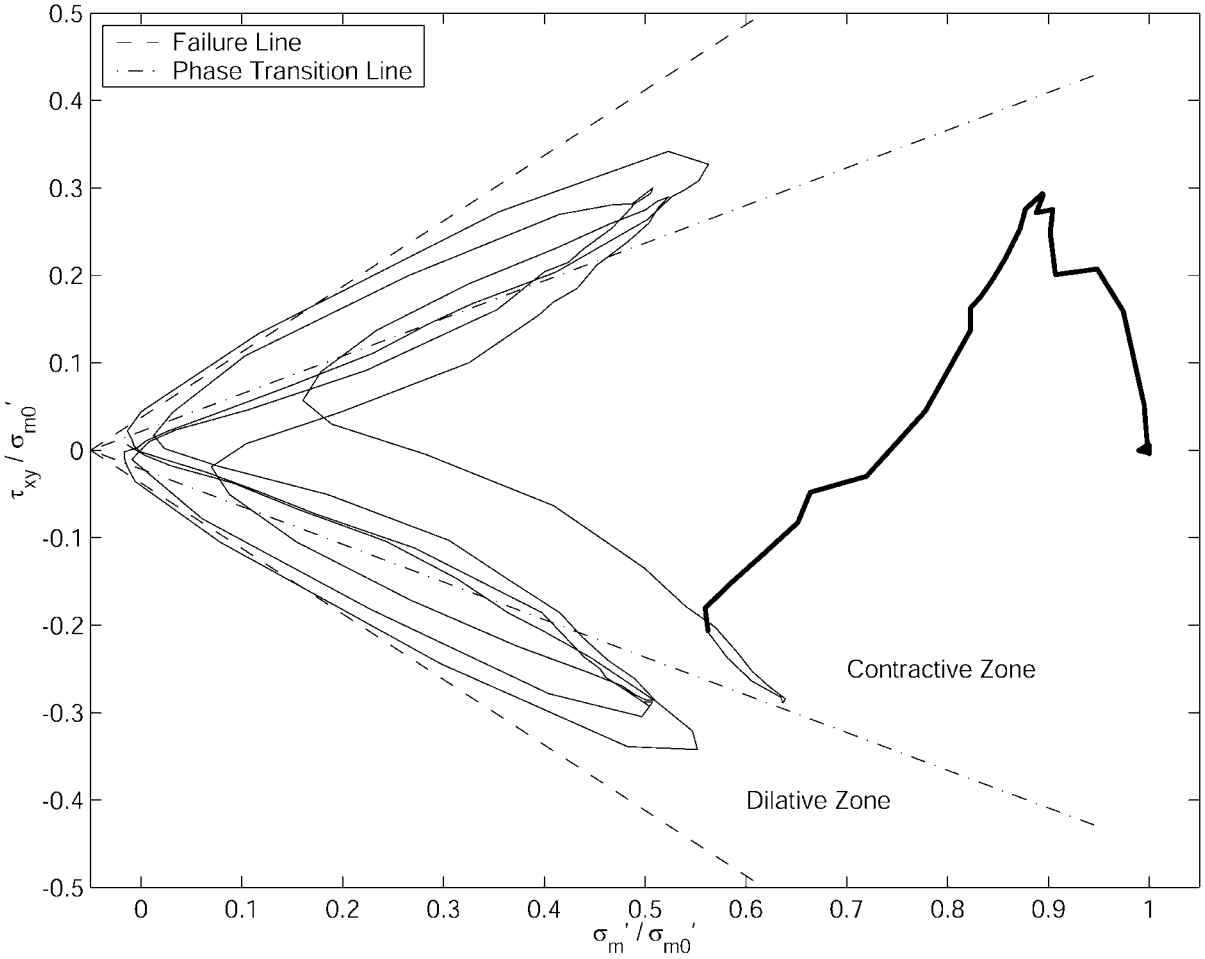

Figure 9. Stress path showing the contractive (thick line) and dilatancy (thin line) zones during a simple shear stress controlled experiment on a dense sand (Arulanandan and Scott, 1993). The effective mean stress is reduced as the time increases. Time evolution is from right to left.

Effect of the Dilatancy in the Stress Wavefield

In soil dynamics, the dynamic behavior of sands is represented by plotting the ratio between the shear stress and the effective confining pressure (effective mean stress) versus the number of cycles to cause 5% deformation peak to peak for an undrained stress controlled experiment (e.g., Fig. 13). This figure shows that the number of cycles needed to cause large deformations decreases proportionally to the stress ratio. When the shear stress is close to the confining pressure, fewer cycles are needed before the soil experiences large deformations. This curve is known as the liquefaction resistance curve. A single number R_{20} is usually taken from this curve. It corresponds to the stress ratio for which the 20 cycles are needed to produce 5% deformation (Ishihara, 1996).

As an example we show the computed liquefaction resistance curve for the soil deposit at the Wildlife Refuge vertical array (Fig. 13). The dilatancy parameters for the calculation are shown in Table 1.

The strength and dynamic properties of dilatant soils have a pronounced effect on seismic waves. We can study this behavior by selecting a soil with a specific stress ratio curve and observe the computed stress at different depths for a given strain time history. We do this because acceleration is the spatial derivative of the stress; by knowing the effect of nonlinearity on the stress time series, we can learn the effect on the acceleration as well. Moreover, lithostatic pressure of the soil element is directly translated into the effective confining pressure. We will study the effects of an irregular strain time history applied at depths of 5, 30, 50, and 100 m. The strain time history is the one computed at GL-2.9 m for the Superstition Hills event. The maximum strain amplitude is 1% for all cases. The stress is computed using the constitutive equation directly. There is no wave propagation in this case. Figure 14 shows the computed stress, stress path, and stress-strain loops. In this figure, the effective mean stress σ_m' is normalized with respect to the initial effective confining pressure σ_{m0}' at each depth, so that

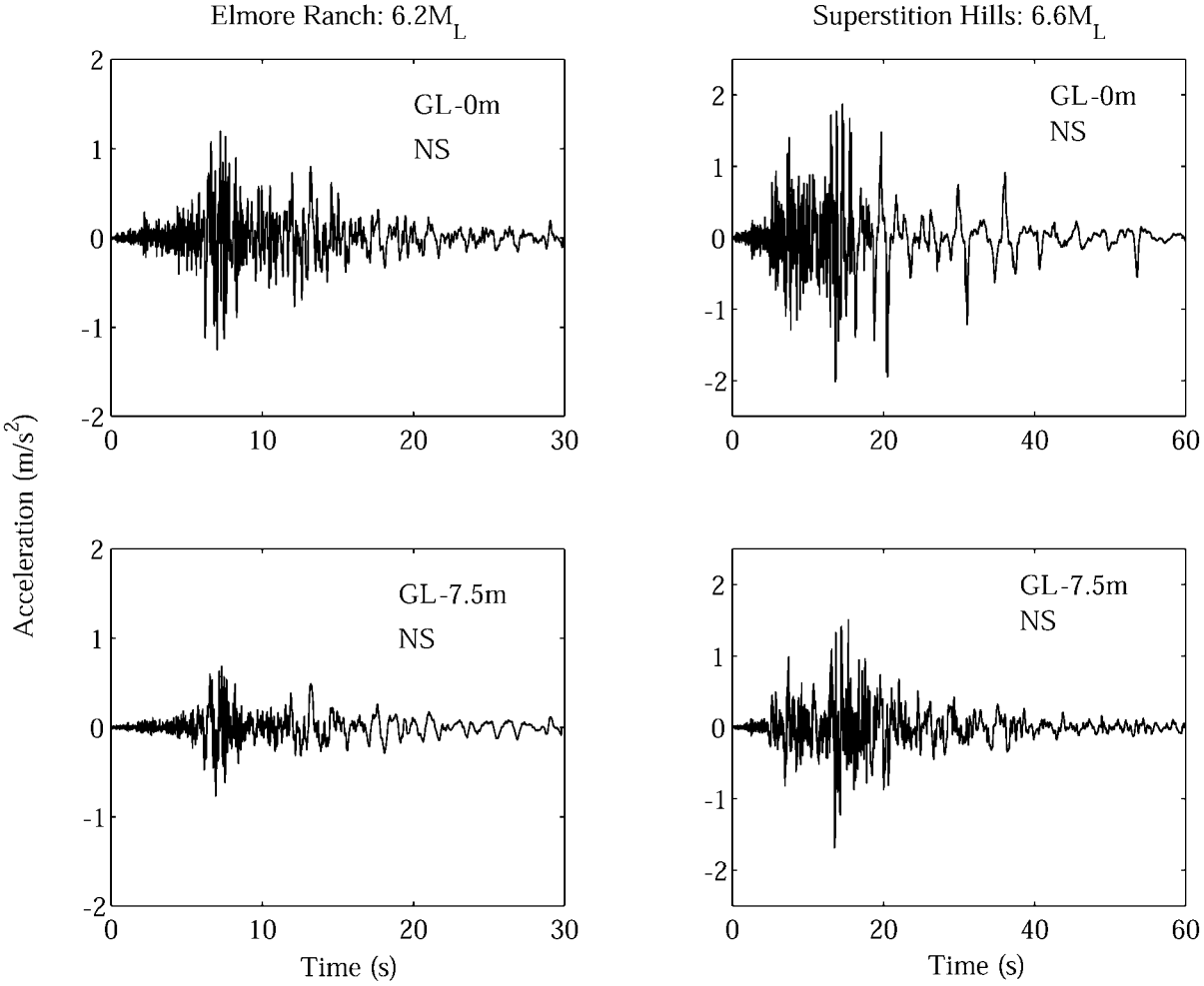

Figure 10. Acceleration time histories for the M_L 6.2 Elmore Ranch and M_L 6.6 Superstition Hills events, both recorded at the Wildlife Refuge station.

all stress paths can be shown at the same scale. Several remarks can be made. The effective mean stress is reduced less at GL-100 m than close to the surface. This should be expected since the soil is stronger at larger depths. A critical feature is the increasing stress path recovery for depths of 30 m and less; it demonstrates that dilatancy is most likely to occur at shallow depths. The stress-strain loops show mostly monotonic modulus degradation with increasing depth. That is, the material behaves mostly contractive; whereas at 5-m depth, the stress-strain phase forms S-shape loops similar to the ones observed in Figure 11. Finally, the computed shear stresses show an increasing spiky (high-frequency content) behavior for shallower depths. This is contrary to the expected nonlinear behavior that leads to deamplification and low-pass filtering of acceleration records. The behavior of the soil suggests that a dilatant material will increase both the amplitude and duration of the strong motion.

In the geotechnical earthquake engineering community many of the effects and characteristics of dilatant soils were known. For example, in the VELACS Project (Arulanandan and Scott, 1993), there are numerous examples of soil rheologies that take into account the cyclic mobility of sands. However, there were few *in situ* data that have been studied. As shown by Archuleta (1998) there are more examples of this behavior as discussed earlier.

Zeghal and Elgamal (1994) analysis of the Wildlife Refuge records explained the spiky acceleration waveforms in relation to dilatant characteristics of the soil. In the analysis of the Kushiro Port records, Iai *et al.* (1995) already shows that cyclic mobility of the sand is the principal mechanism for producing such characteristic waveforms.

In the next two sections, we reanalyze the records from the 1993 Kushiro-Oki and the 1987 Superstition Hills earthquakes in order to understand the effect of nonlinearity of dilatant soils caused by wave propagation.

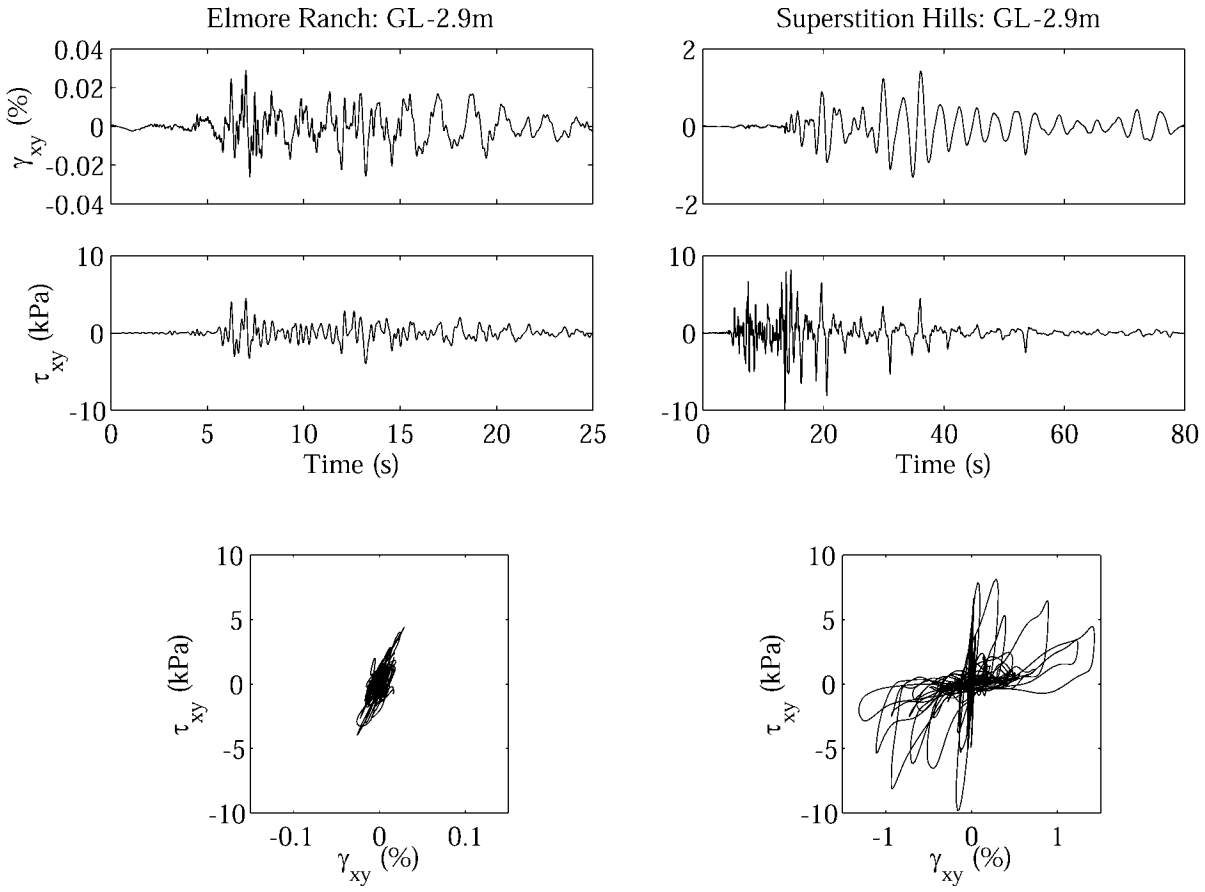

Figure 11. North–south stress and strain time histories, and strain-stress curves at GL-2.9 m for the Elmore Ranch and Superstition Hills earthquakes. The waveforms are low-pass filtered at 5 Hz.

The 1993 Kushiro-Oki Earthquake

The *M* 7.8 Kushiro-Oki earthquake occurred on 15 January 1993 with a hypocenter at a depth of 105 km. Its epicenter was about 15 km south of Kushiro City, Japan. A vertical array at Kushiro Port recorded this event. This array has two accelerometers: a GL-77 m downhole and GL-0 m triaxial accelerometers (Iai *et al.*, 1995). We plot the surface and downhole accelerograms in Figure 2. Note the spiky repetitive waveform that dominates the north–south surface component around 25 sec after the start time.

We revisit the Kushiro-Oki data in order to compare our modeling approach with that presented by Iai *et al.* (1995). In this way we can validate the hysteresis operator (Bonilla, 2000) with a more complex rheology. With this we can examine some problems related to modeling nonlinearity in soils, such as the values of the geotechnical parameters and the accuracy of the numerical method for nonlinear wave propagation. It is worth mentioning that Iai *et al.*'s (1995) analysis of these data was a validation test of their method as well. They never intended to find a perfect fit to the observed data; the analysis was to validate their technique as a method to predict nonlinear soil behavior in liquefaction prone areas from future events.

Geotechnical Information

One of the major difficulties for nonlinear modeling is the need for additional material parameters in addition to those used in linear wave propagation. Even under dry conditions (no pore pressure), we need the maximum strength of the material. This problem worsens when the analysis is effective stress analysis (pore pressure effect). Towhata and Ishihara (1985) and Iai *et al.* (1990a) model accounts for the pore pressure evolution. It is one of the simplest methods to use and requires only five dilatancy parameters as mentioned in section about the soil constitutive model.

Cores from the Kushiro Port vertical array were carefully sampled and tested (Iai *et al.*, 1995). The soil deposit consists of a dense sand. The soil column is divided in eight layers whose material properties are listed in Table 2. The water table is found at GL-2 m depth. Only the first two layers beneath the water table are thought capable of gen-

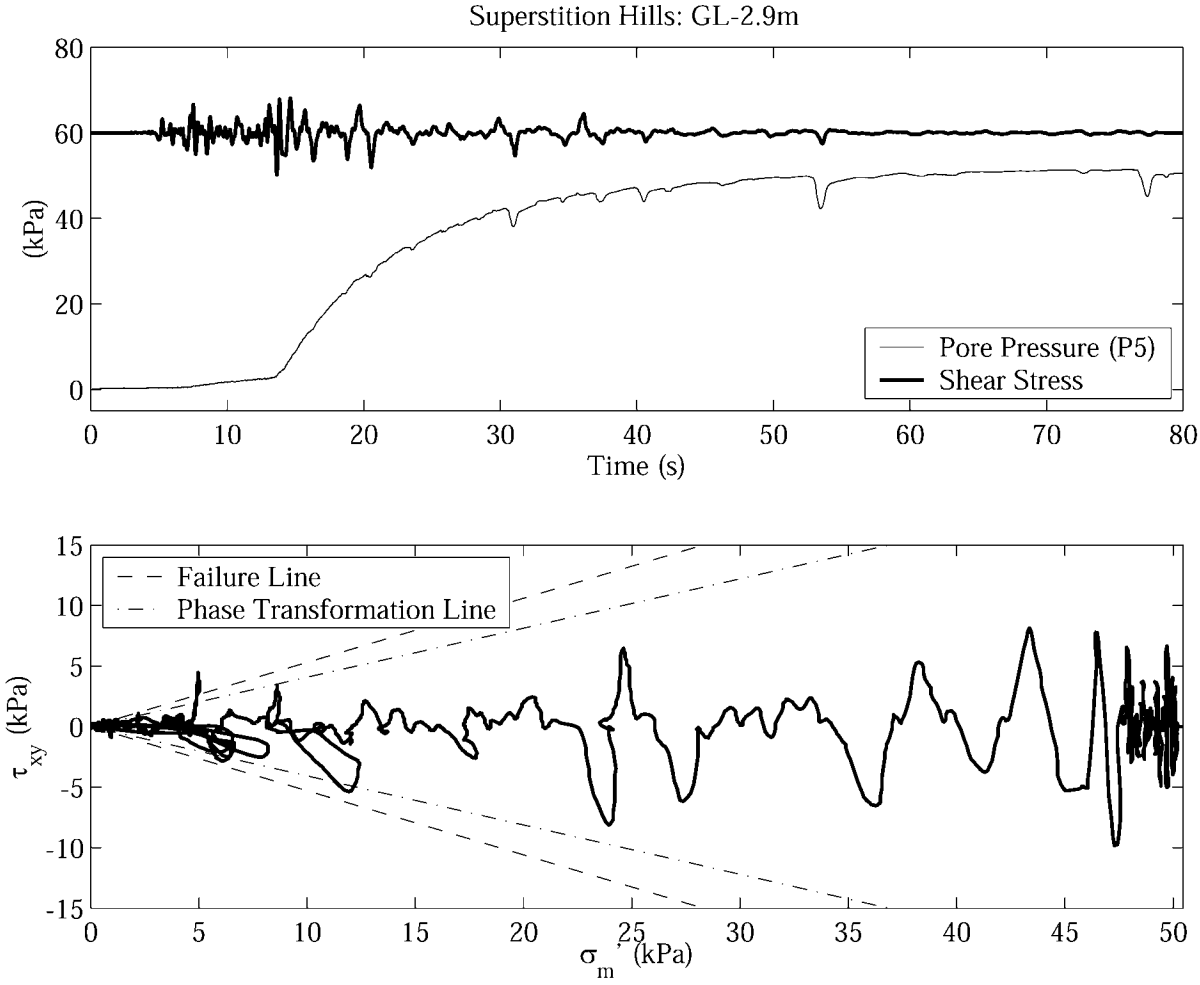

Figure 12. Shear stress and pore pressure from transducer P5 (top). Reconstructed stress path (bottom). The failure and phase transformation lines are those proposed by Zeghal *et al.* (1996).

erating pore pressure (Table 3) because the underlying layers have significantly larger liquefaction resistance.

Results

At any depth, the particle motion contains the incident wavefield, reflections from the free surface as well as from the different velocity interfaces in the soil column. Thus, when a downhole record is available, most nonlinear studies make use of it as a rigid boundary condition, that is, the motion at the boundary is specified at any given time by the downhole record. Conversely, when the input motion is the incident wavefield only (e.g., outcrop record) the boundary corresponds to an elastic or transmitting boundary condition because some energy coming back from the downgoing wavefield will be transmitted to the underlying medium (Joyner and Chen, 1975).

Figure 15 shows the computed ground motion at the surface and their 5% response spectra when the borehole record is used as an input motion at GL-77 m. The computation was done with a maximum frequency of 10 Hz, 25 points per wavelength (1.0-m grid spacing), and $dt = 5.0 \times 10^{-4}$ sec. The recorded motions are shown with no filtering; whereas the computed one is lowpass filtered below 10 Hz.

To date, there is no single method to describe the universal goodness of fit for a time series. Usually waveforms are compared by eye. Although we will consider the appearance of the waveforms, we also use the acceleration response spectra.

The result (Fig. 15) shows a good fit in the time domain where all observed features of the nonlinear soil behavior have been captured, for example, the spikes in the accelerogram around and after 25 sec. Although the timing and phase of such spikes are well simulated, the observed PGA has not been achieved. The response spectra show that the record at GL-77 m depth is rich in short periods (high frequencies). With soil nonlinearity the frequency content shifts

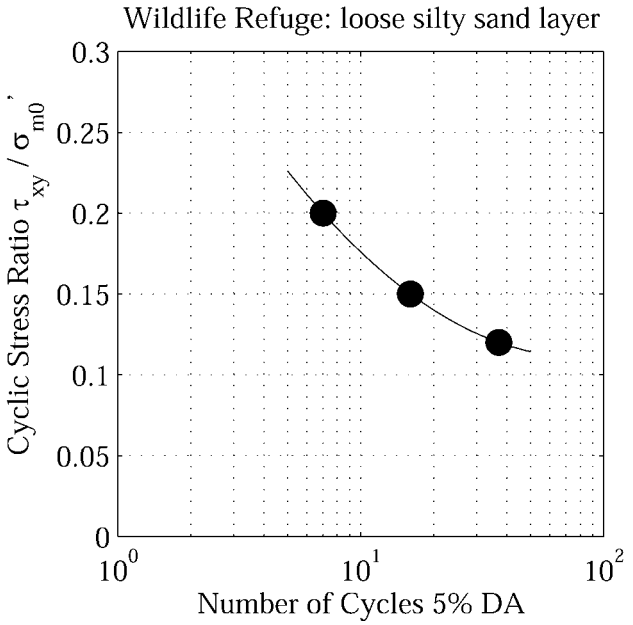

Figure 13. Simulated liquefaction resistance curve for the loose silty sand layer at the Wildlife Refuge site. The dilatancy parameters are shown in Table 1.

Table 1
Dilatancy Parameters for the Loose Silty Sand Layer at the Wildlife Refuge Vertical Array

β (m/sec)*	σ'_{m0} (kPa)	ϕ	ϕ_p	w_1	p_1	p_2	c_1	S_1
116.0	53.7	32.0	24.0	4.0	0.4	0.9	2.0	0.01

*Shear-wave velocity.

to longer periods (lower frequencies). In addition, this shift occurs with a large amplification around 1 sec. Full amplification is not reached during the simulation. We could find other dilatancy parameters that better fit the observations. However, this fitting procedure is left for another event, the Wildlife Refuge record instead.

Stability of the Numerical Solution

Any numerical solution of the wave equation has to comply with the so-called stability conditions. These are numerical constraints that keep the numerical solution stable (no divergence with time) and accurate. The stability conditions are for both discretization grid *dy* and time step *dt*. For the one-dimensional wave propagation case they are (Aki and Richards, 1980)

$$dy = \frac{V_{\min}}{f_{\max}\, ppw}$$

$$dt = p_0 \frac{dy}{V_{\max}},$$

where $V_{\max}$ and $V_{\min}$ are the maximum and minimum velocity of the medium, *ppw* is the number of points per wavelength, $f_{\max}$ is the maximum frequency of the simulation, and p_0 is the fraction of the minimum timestep.

Numerical solutions of the linear wave equation uses between 6 and 12 points per wavelength depending on the numerical scheme used. For instance, for a second-order scheme the number is 12, and for fourth-order scheme the number is 6 (Aki and Richards, 1980). However, in the case of nonlinear wave propagation more points per wavelength are needed to avoid dispersion of the solution.

In nonlinear materials the shear modulus *G* decreases as the shear strain increases. Since the shear modulus $G = \rho\beta^2$, a decrease in the modulus reduces the effective shear-wave speed as well, and thus more points per wavelength are needed to make the solution stable. The value of p_0 controls the fraction of the timestep so that the numerical solution has the correct phase.

The effective grid spacing should be computed using the final value of the material velocity after it has experienced nonlinearity. This, of course, is not possible to do *a priori*. However, a first approximation can be made by choosing a convenient number of points per wavelength *ppw*, and a p_0 value.

In the present computation, we chose a grid spacing of 1 m, which corresponds to 25 points per wavelength. Then, we compute solutions for different values of p_0. We do this to observe the accuracy of the stress-strain computation as a function of the selected time step. Four sets of different points per wavelength were used in the computations. The associated grid distances *dy* and time steps *dt* are listed in Table 4.

Figures 16 and 17 show computed acceleration time histories at GL-0 m and maximum shear strain versus depth for different values of p_0. All computed results are low-pass filtered (butterworth filter, 4 poles) below 10 Hz. The original observation at GL-0 m is shown unfiltered. It is worth noting that the lower the p_0 values, the stronger the dilatancy pulses at the end of the accelerogram. One possible explanation is that the shear modulus is highly reduced due to the pore pressure development late in the record. Thus, reducing the timestep during the computation may align the phase of pulses that arrive late due to the dilatancy of the material.

The strain depth distribution shows that the maximum strain is reached at shallow depth: this is expected since the shear strength of the soil at these depths is smaller. Note the largest difference among the different computations occurs at these depths. Indeed, when pore pressure is not important as in the case of layers deeper than GL-23 m, the computed strains are quite stable for large values of p_0. This cannot be generalized because the input motion in this case was not very large.

Figure 18 shows examples of the stress-strain loops and mean effective stress reduction at GL-3 m depth for values of $p_0 = 0.34$ and $p_0 = 0.17$, respectively. We observe that the stress-strain hysteresis loops are *smoother* for the latter

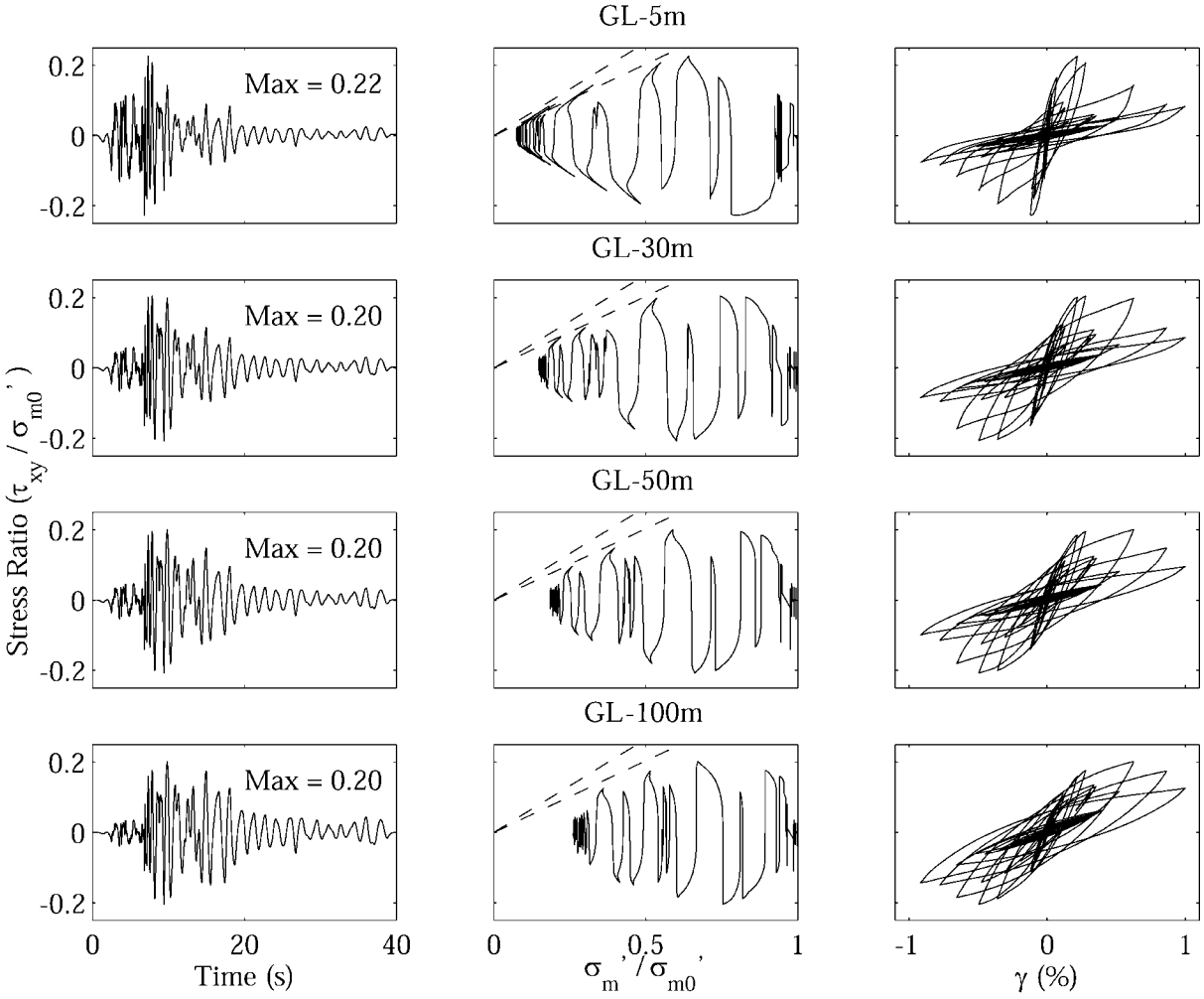

Figure 14. Shear-stress, stress-path, and stress-strain curves computed when the input is the irregular strain time history computed at GL-2.9 m for the Superstition Hills event. The input is normalized to a maximum deformation of 1% for all cases. The dashed lines represent the failure and phase transformation lines, respectively. The soil is the one described by the liquefaction resistance curve in Figure 13.

value of p_0. It is not clear if this is a better solution than any other solution. However, when $p_0 = 0.17$, the loops do not have as much as high-frequency content. This suggests that the result will not have any spurious noise when small enough timesteps are used.

Iai *et al.* (1995) reported deformations up to 1.5% at GL-3.5 m. They used a finite-element implementation for the numerical solution of the wave propagation. In their study, the grid spacing is divided into elements of 1-m thickness; the time step is 0.01 sec. The integration is done by the Wilson-θ method ($\theta = 1.4$) with Rayleigh damping of $\beta = 0.0005$. They performed sensitivity analysis on the dilatancy parameters but not on the numerical model. We obtained different results for all models we used. Nonetheless the fit to the observed record at the surface is reasonably good for all these models as well. Further research is needed in terms of finite-element and finite-difference techniques to solve this nonlinear problem.

The 1987 Superstition Hills Earthquake

On 24 November 1987, the M_L 6.6 Superstition Hills earthquake was recorded at the Wildlife Refuge station. This site is located in southern California in the seismically active Imperial Valley. In 1982 it was instrumented by the U.S. Geological Survey with downhole and surface accelerometers and piezometers to record ground motions and pore water pressures during earthquakes (Holzer *et al.*, 1989).

The Wildlife site is located in the flood plain of the Alamo River, about 20 m from the river's western bank. *In situ* investigations have shown that the site stratigraphy consists of a shallow silt layer approximately 2.5 m thick underlain by a 4.3 m thick layer of loose silty sand, which is in turn underlain by a stiff to very stiff clay.

The water table fluctuates around 2-m depth (Matasovic and Vucetic, 1993). Vucetic and Thilakaratne (1989) proposed a velocity profile for the site. They used seven layers

Table 2
Material Properties Model for the Kushiro Port Vertical Array (TEN After Iai *et al.*, 1995)

Layer	Depth (m)	σ'_{ma} (kPa)*	β (m/sec)	ρ (kg/m^3)	ϕ	ϕ_p	K_0†	ξ_{max}‡
1	0–2	36.6	249	1720	40	—	0.5	0.3
2	2–9	36.6	249	1720	40	28	0.5	0.3
3	9–23	97.9	326	1980	48	28	0.5	0.3
4	23–32	164.3	265	1730	37	—	0.5	0.3
5	32–36	195.7	341	1760	44	—	0.5	0.3
6	36–42	219.4	286	1700	44	—	0.5	0.3
7	42–50	259.3	302	2000	45	—	0.5	0.3
8	50–77	349.9	341	1730	44	—	0.5	0.3

*Effective mean stress computed at the middle of each soil layer.
†K_0 is the so-called coefficient of earth at rest: it represents the horizontal to vertical ratio of the initial effective normal stresses
‡ξ_{max} is the maximum hysteretic damping ratio at large strains.

Table 3
Dilatancy Parameters at Kushiro Port Vertical Array

Layer	w_1	p_1	p_2	c_1	S_1
2	7.0	0.5	0.65	3.97	0.01
3	3.5	0.5	0.4	3.68	0.01

After Iai *et al.* (1995).

Table 4
Grid Size and Timestep Used in the Kushiro-Oki Event Stability Analysis

p_0	dy (m)	dt* (s)
0.85	1.0	2.5×10^{-3}
0.68	1.0	2.0×10^{-3}
0.34	1.0	1.0×10^{-3}
0.17	1.0	5.0×10^{-4}

*$ppw = 25$.

for their numerical modeling. Conversely, Gu *et al.* (1994) simplified the velocity structure of the soil units to the ones listed Table 5. The water table depth is assumed at GL-1.5 m as Gu *et al.* (1994) proposed. The value of the coefficient of earth at rest K_0 is assumed to be equal to 1 (isotropic conditions). The angle of the phase transformation line is 24° as suggested by Zeghal *et al.* (1996). The liquefaction array at the Wildlife site consists of two accelerometers and six electric piezometers. One accelerometer was installed at the surface, and the downhole one was installed in the liquefiable layer at GL-7.5 m depth. Five of the six piezometers were also installed in this sand layer (Youd and Holzer, 1994).

Figure 4 shows the recorded accelerations at the surface and depth. The horizontal accelerograms at GL-0 m show spikes right after the *S* waves have passed. These spikes have reach acceleration levels up to 2 m/sec^2. This phenomenon is more prominent on the north–south component.

Using the stress and stress time histories at GL-2.9 m computed the earlier, we performed a trial-and-error procedure in order to obtain the dilatancy parameters that best reproduce such observations. These parameters are listed in Table 1 and model the dilatancy characteristics of layer 3. Figure 19 compares the computed shear stress time history with the observed shear strain at GL-2.9 m. The stress-strain hysteresis loops are also shown. We observe that the computed shear stress is well simulated; the stress-strain space also shows the same dilatant behavior as the observed data.

Results

Once the model parameters are determined, we proceed to compute the acceleration time history at GL-0 m using the north–south record at GL-7.5 m as input motion. As in the case of the Kushiro-Oki event, the Wildlife downhole record is the dynamic boundary condition for the analysis. The grid spacing has been set to 0.25 m and $dt = 2.0 \times 10^{-4}$ sec. This corresponds to 40 points per wavelength and $p_0 = 0.1$. The maximum frequency of the computation is 10 Hz.

Figure 20 shows the accelerograms (left) and the corresponding response spectra (right). The observed data are shown with no filtering, whereas the computed data are low-pass filtered at 10 Hz. The computed accelerogram shows the transition from high-frequency content between 0 and 15 sec to the intermittent spiky behavior after 15 sec. The response spectra show that the computed accelerogram accurately represents the long periods. The short periods are still difficult to model accurately. The nonlinearity appears too quickly in the model. This can be explained by looking at Figure 21 where the pore pressure ratio at GL-2.9 m is shown for both observed (piezometer P5) and computed data. Indeed, the computed pore pressure ratio grows faster than the observed one. This means that the modulus degradation begins earlier than what might have happened in reality. This figure also shows a pore pressure relaxation beginning at 15 sec and continues to the end of the simulation at 80 sec. This relaxation, due to the dilatancy, is why the computed accelerogram shows spikes late in time.

Finally, in Figure 22 we plot the maximum shear strain versus depth. The maximum deformation is concentrated between 2.5- and 5.5-m depth, reaching values close to 10%. If we follow the convention that 5% deformation implies material failure, then the site liquefied at this depth range.

Conclusions

There is a new direct observation of nonlinearity in dense cohesionless soils: nearly repetitive, high-frequency, large-amplitude spikes late in the acceleration time history. This nonlinearity reveals itself in the accelerograms as seen in the examples shown early in this work. The dilatant nature of dense sands produces the partial recovery of the strength under cyclic loads. This recovery translates into the ability

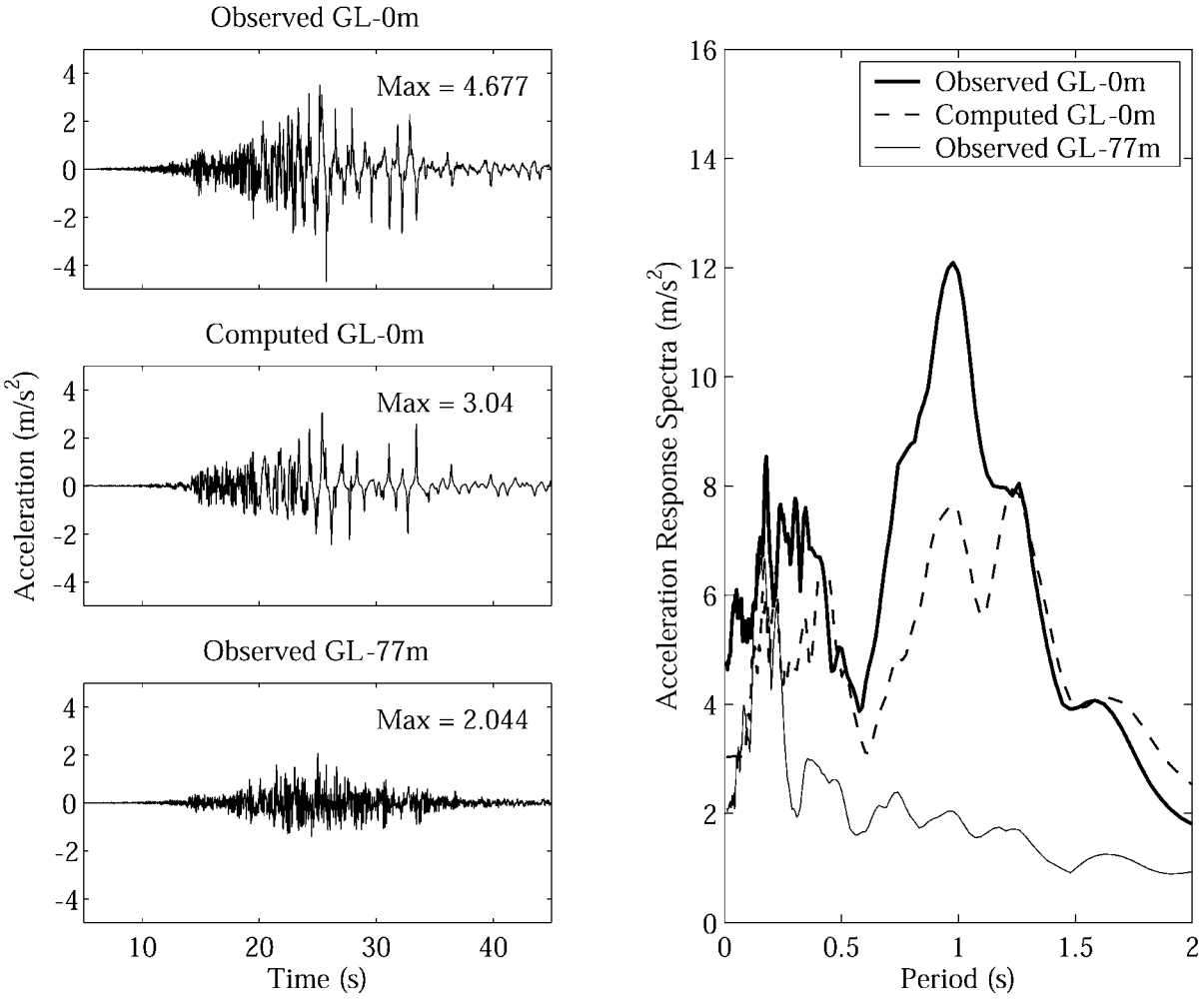

Figure 15. Computed acceleration of the north–south component at GL-0 (left) and the corresponding response spectra (right) when the input motion is the observed record at GL-77 m. The observed data are shown with no filtering, whereas the computed acceleration has been low-pass filtered at 10 Hz.

to produce large deformations followed by large and spiky shear stresses. The spikes observed in the acceleration records are directly related to these periods of dilatancy and generation of pore pressure. These results are significant in strong-motion seismology because these spikes are site related; they do not come from the source.

As expected, the numerical solutions demonstrate a shift of the time series frequency content to lower frequencies as the degree of nonlinearity is increased. Nonetheless, there is also a broadband amplification. As a consequence, this phenomenon increases the duration of the strong shaking and in some circumstances produces the maximum acceleration. Broadband amplification and increasing duration of strong shaking are not normally associated with the effects of nonlinearity.

The accuracy and stability of the numerical solution of the wave propagation, when large deformations are present, strongly depend on the grid spacing and timestep chosen for the finite-difference scheme. Numerical examples for the Kushiro-Oki earthquake show that the computed deformations are very sensitive to these factors. Unless an adaptive meshing and timestepping procedure is used, solution for different values of grid space and timestep should be evaluated.

In the course of modeling these events, the benefit of the acceleration response spectra, as a goodness of fit estimator, became clear. The response spectra is sensitive to the energy content on the whole record. It shows where the spectral energy is located. Sometimes, when the time series are similar—even the peak values are close—their response spectra are different.

Finally, site effect studies that attempt to isolate nonlinearity using the average spectral ratios of weak and strong ground motion may not give the correct answer. Nonlinear behavior of dilatant materials shows a broadband spectrum compared to purely contractive soils. Thus the averaging

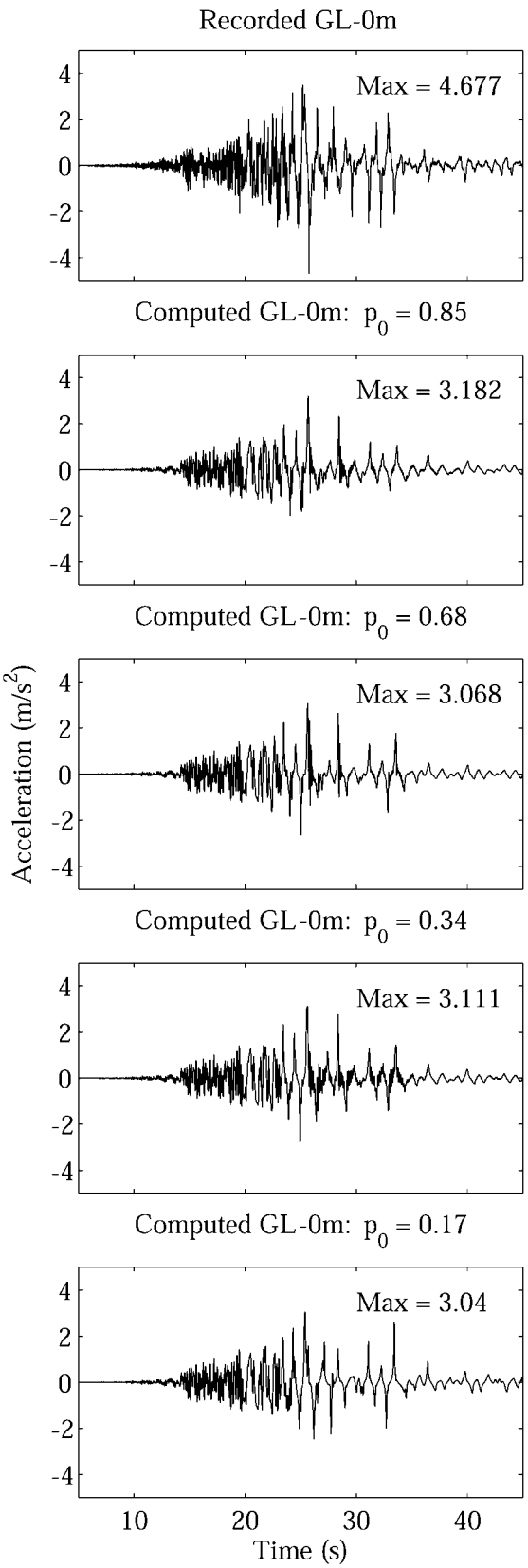

Figure 16. Computed acceleration of the north–south component at GL-0 for different values of p_0 when $ppw = 25$ (1.0 m grid spacing). The input motion is the recorded accelerogram at GL-77 m.

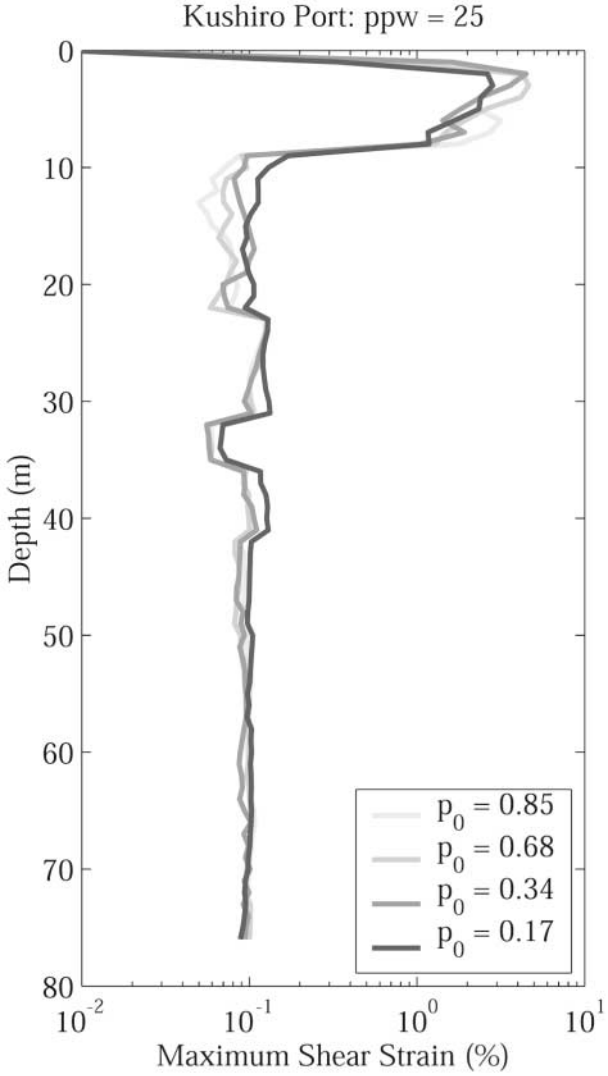

Figure 17. Distribution of the maximum shear strain versus depth for different values of p_0 when $ppw = 25$ (1.0-m grid spacing). Note the development of the deformation between 3- and 9-m depth.

Table 5
Material Properties Model for the Wildlife Refuge Site

Layer	Depth (m)	σ'_{ma} (kPa)	β (m/sec)	ρ (kg/m^3)	ϕ	ϕ_p	K_0	ξ_{max}
1	0–1.5	11.7	99	1600	28	—	1.0	0.3
2	1.5–2.5	28.1	99	1928	28	—	1.0	0.3
3	2.5–6.8	53.7	116	2000	32	24	1.0	0.3
4	6.8–7.5	78.2	116	2000	32	—	1.0	0.3

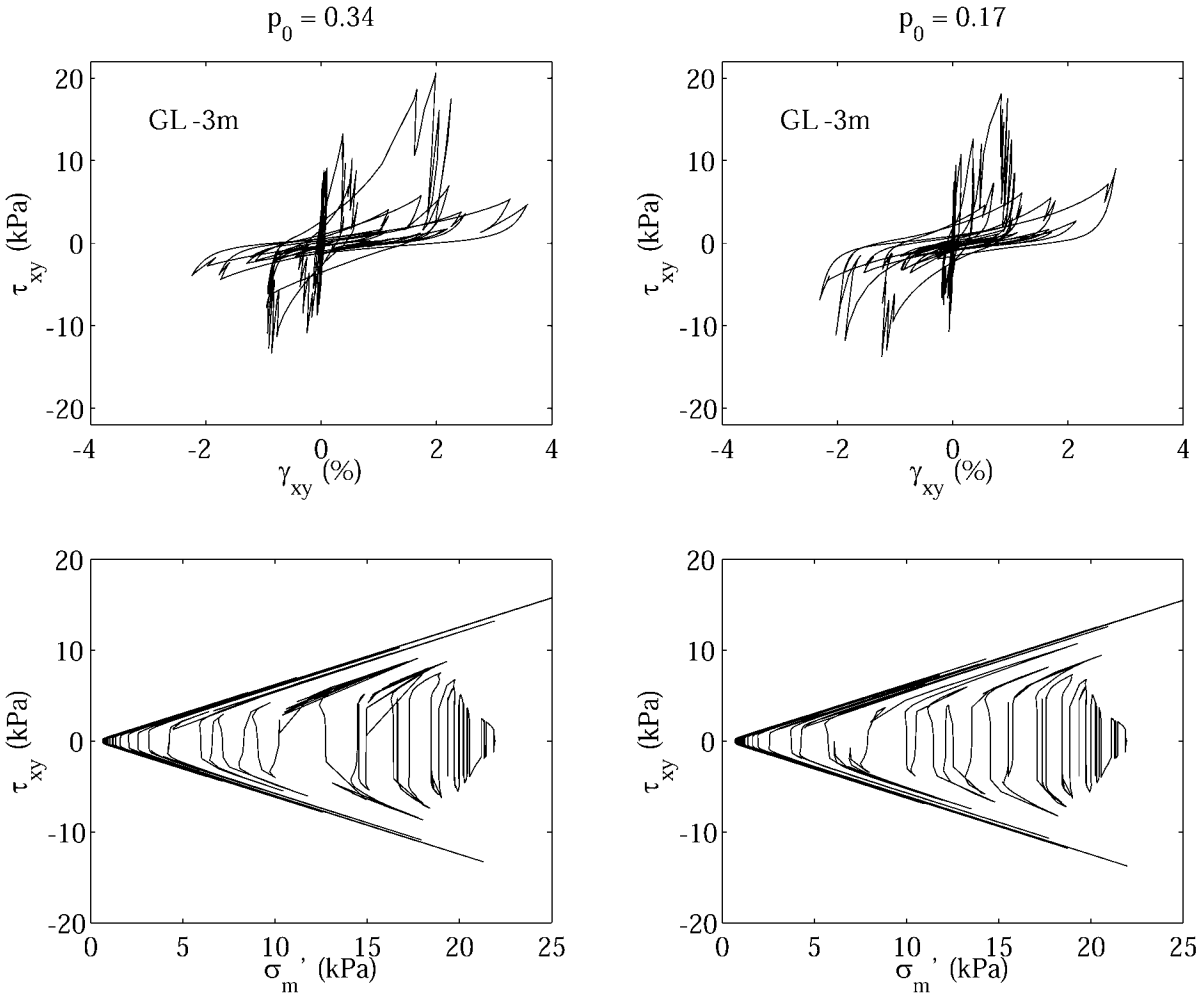

Figure 18. Stress-strain loops and stress paths at GL-3 m when $ppw = 25$ (1.0-m grid spacing) for two values of p_0.

may actually hide the nonlinearity based solely on one class of behavior.

Acknowledgments

The authors are in debted to Dr. Susumu Iai, who kindly provided the acceleration time histories of the Kushiro-Oki earthquake and answered our many questions in helping us implement his rheology model. We would like to express our gratitude to Dr. Stefan Nielsen and Dr. Peng-Chen Liu, who helped us with programming the finite-difference scheme and implementing Q in the code. L.F.B. is also very grateful to Dr. Steve Hartzell, who through long discussions and tests of the codes, helped to finish the current version of the finite-difference computer program. We greatly appreciate the comments of Dr. Igor Beresnev and two anonymous reviewers for their help in improving the clarity of this work. Finally, the computer code is available upon request.

References

Aguirre, J., and K. Irikura (1997). Nonlinearity, liquefaction, and velocity variation of soft soil layers in Port Island, Kobe, during the Hyogo-ken Nanbu Earthquake, *Bull. Seism. Soc. Am.* **87,** 1244–1258.

Aki, K. (1993). Local site effects on weak and strong ground motion, *Tectonophysics* **218,** 93–111.

Aki, K., and P. G. Richards (1980). *Quantitative Seismology: Theory and Methods*, W. H. Freeman and Company, San Francisco, 932 pp.

Archuleta, R. J. (1998). Direct observation of nonlinearity in accelerograms, in *The Effects of Surface Geology on Seismic Motion*, Vol. 2, K. Irikura, K. Kudo, H. Okada, and T. Sasatami (Editors), Balkema, Rotterdam, 787–792.

Arulanandan, K., and R. F. Scott (1993). *Verification of Numerical Procedures for the Analysis of Soil Liquefaction Problems*, 2 Vols., K. Arulanandan and and R. F. Scott (Editors), A.A. Balkema, The Netherlands.

Bardet, J. P., and C. Davis (1996). Engineering observations on ground motion at the Van Norman Complex after the 1994 Northridge earthquake, *Bull. Seism. Soc. Am.* **86,** no. 1B, S333–S349.

Beresnev, I. A., and K. L. Wen (1996). Nonlinear site response—a reality? *Bull. Seism. Soc. Am.* **86,** 1964–1978.

Beresnev, I. A., K. L. Wen, and Y. T. Yeh (1995). Nonlinear soil amplification: its corroboration in Taiwan, *Bull. Seism. Soc. Am.* **85,** 496–515.

Bonilla, L. F. (2000). Computation of linear and nonlinear site response for near field ground motion, *Ph.D. Thesis*, University of California, Santa Barbara.

Field, E. H., P. A. Johnson, I. A. Beresnev, and Y. Zeng (1997). Nonlinear

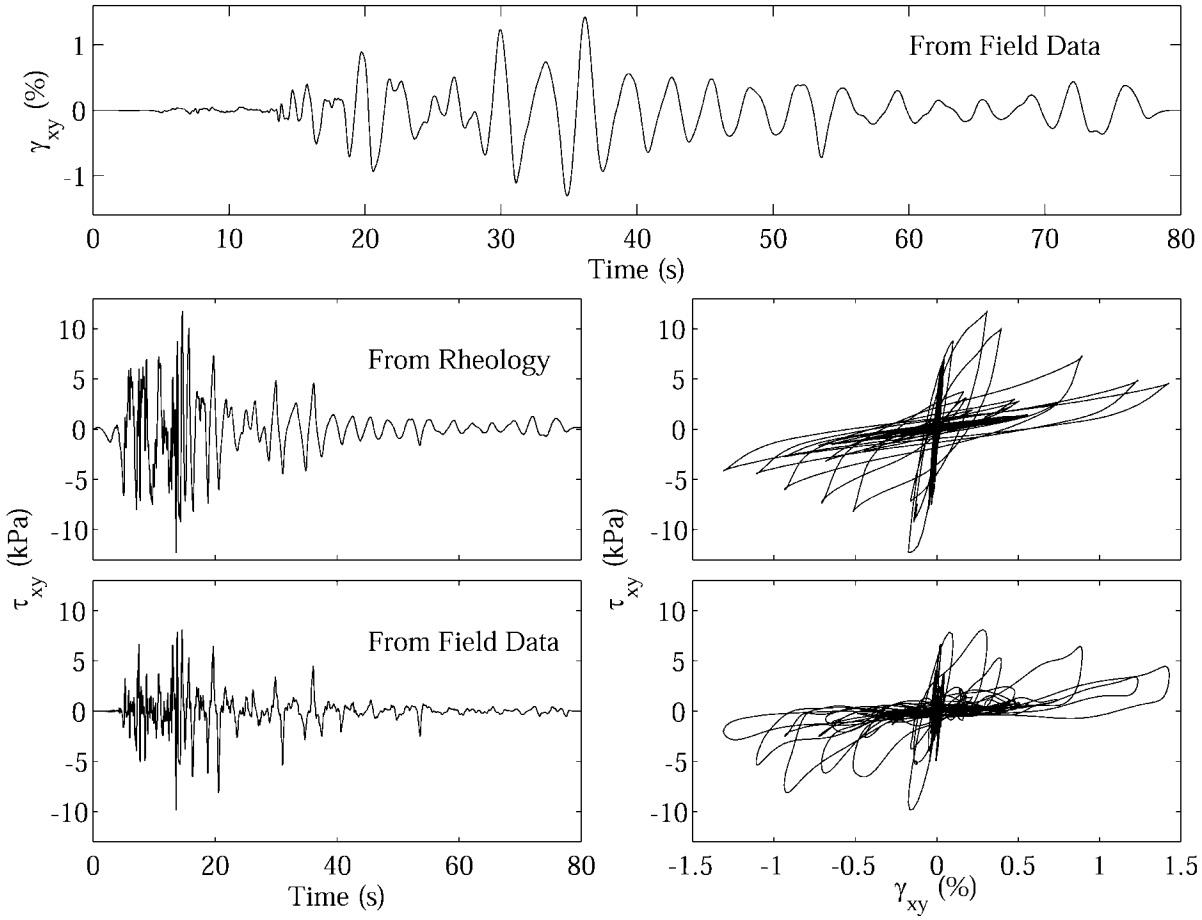

Figure 19. Computed shear stress when using the deduced shear strain as input. The corresponding hysteresis loops are also shown.

ground-motion amplification by sediments during the 1994 Northridge earthquake, *Nature* **390,** 599–602.

Frankel, A. D., D. L. Carver, and R. A. Williams (2002). Nonlinear and linear site response and basin effects in Seattle for the M 6.8 Nisqually, Washington earthquake, *Bull. Seism. Soc. Am.* **92,** 2090–2109.

Gu, W. H., N. R. Morgenstern, and P. K. Robertson (1994). Postearthquake deformation analysis of Wildlife site, *J. Geotech. Eng.* **120,** no. 2, 274–289.

Hardin, B. O., and V. P. Drnevich (1972a). Shear modulus and damping in soil: measurement and parameter effects, *J. Soil Mech. Found. Div. ASCE* **98,** 603–624.

Hardin, B. O., and V. P. Drnevich (1972b). Shear modulus and damping in soil: design equations and curves, *J. Soil Mech. Found. Div. ASCE* **98,** 667–692.

Hartzell, S. H., (1978). Earthquake aftershocks as Green's functions, *Geophys. Res. Lett.* **5,** 1–4.

Hartzell, S. H., L. F. Bonilla, and R. A. Williams (2004). Prediction of nonlinear soil effects, *Bull. Seism. Soc. Am.* **94,** 1609–1629.

Holzer, T. L., T. L. Youd, and T. C. Hanks (1989). Dynamics of liquefaction during the 1987 Superstition Hills, California, earthquake, *Science* **244,** 56–59.

Hutchings, L. (1991). "Prediction" of strong ground motion for the 1989 Loma Prieta earthquake using empirical Green's functions, *Bull. Seism. Soc. Am.* **81,** 1813–1837.

Iai, S., Y. Matsunaga, and T. Kameoka (1990a). Strain space plasticity model for cyclic mobility, *Report of the Port and Harbour Research Institute*, **29,** 27–56.

Iai, S., Y. Matsunaga, and T. Kameoka (1990b). Parameter identification for cyclic mobility model, *Report of the Port and Harbour Research Institute*, **29,** 57–83.

Iai, S., T. Morita, T. Kameoka, Y. Matsunaga, and K. Abiko (1995). Response of a dense sand deposit during 1993 Kushiro-Oki Earthquake, *Soils Found.* **35,** 115–131.

Idriss, I. M. (1990). Response of soft soil sites during earthquakes, in *Proceedings of the H. Bolton Seed Memorial Symposium*, Vol. 2, J. M. Duncan (Editor), BiTech Publishers, Vancouver, 273–289.

Idriss, I. M., and H. B. Seed (1968). Analysis of ground motions during the 1957 San Francisco earthquake, *Bull. Seism. Soc. Am.* **58,** 2013–2032.

Ishihara, K. (1996). *Soil Behaviour in Earthquake Geotechnics*, Clarenton Press, Oxford, 350 pp.

Ishihara, K., and I. Towhata (1982). Dynamic response analysis of level ground based on the effective stress method, *in Soil Mechanics—Transient and Cyclic Loads*, G. N. Pande and and O. C. Zienkiewicz (Editors), 133–172.

Iwan, W. D. (1967). On a class of models for the yielding behavior of continuous and composite systems, *J. Appl. Mech.* **34,** 612–617.

Iwasaki, Y., and M. Tai (1996). Strong motion records at Kobe Port Island, *Special Issue of Soils and Foundations*, Japanese Geotechnical Society, 29–40.

Jaeger, J., and N. G. W. Cook (1979). *Fundamentals of Rock Mechanics*, Third Edition, Chapman and Hall, London, 593 pp.

Joyner, W., and A. T. Chen (1975). Calculation of nonlinear ground response in earthquakes, *Bull. Seism. Soc. Am.* **65,** 1315–1336.

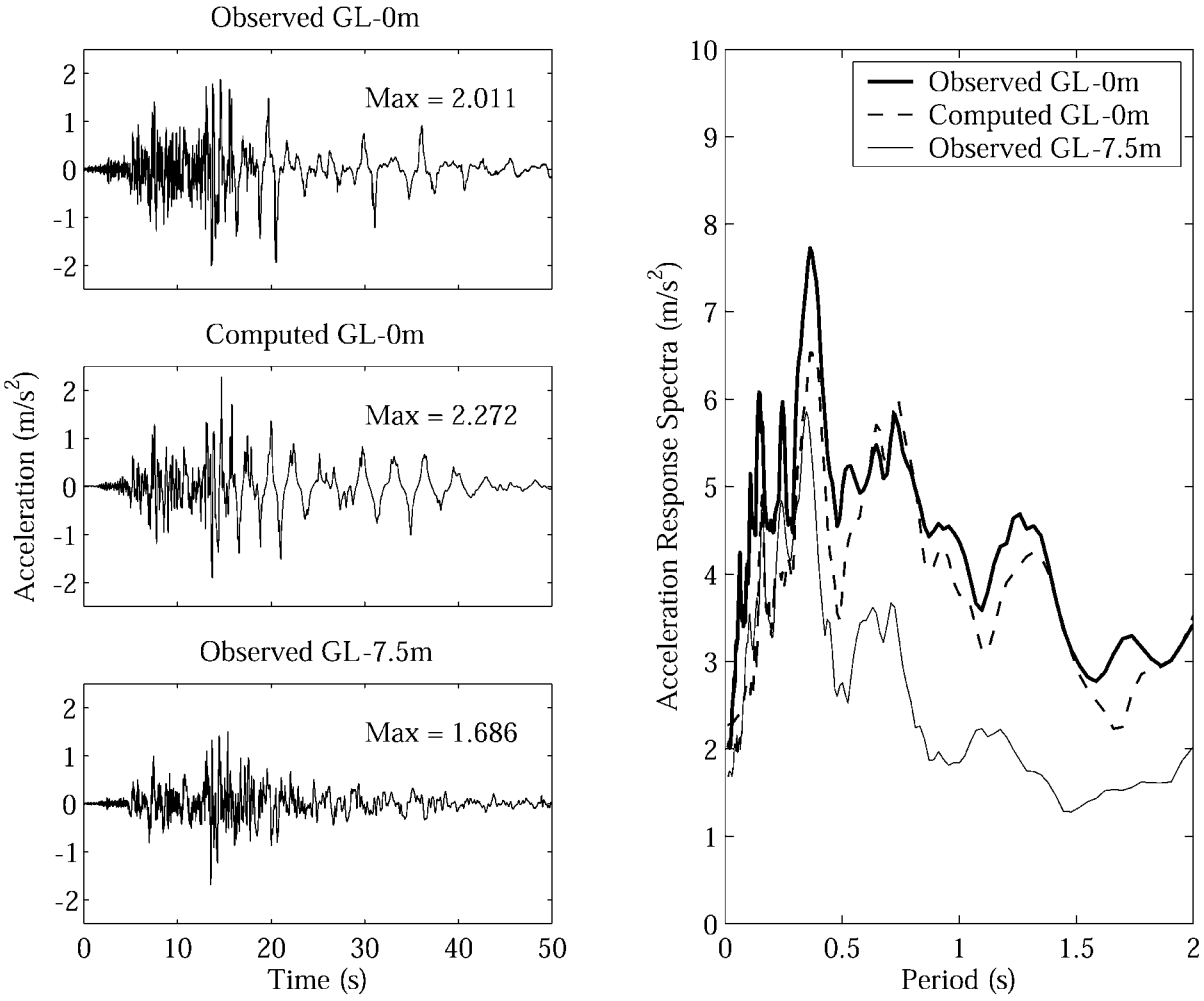

Figure 20. Acceleration time histories (left) and their corresponding response spectra (right) for the north–south component of the Superstition Hills record at the Wildlife Refuge site. The observed acceleration records are shown without filtering. The computed acceleration has been low-pass filtered at 10 Hz.

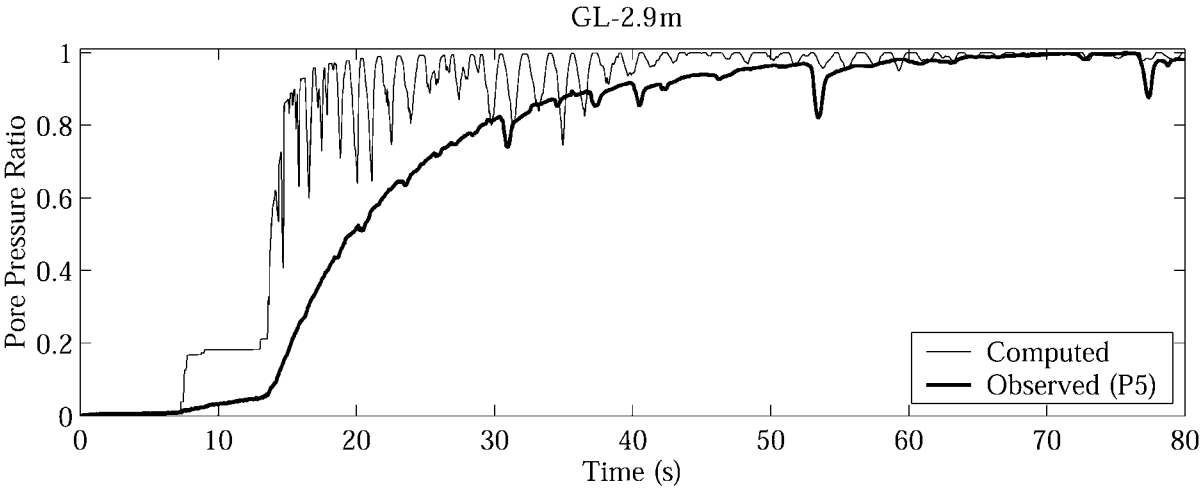

Figure 21. Computed and observed pore pressure ratios at GL-2.9 m.

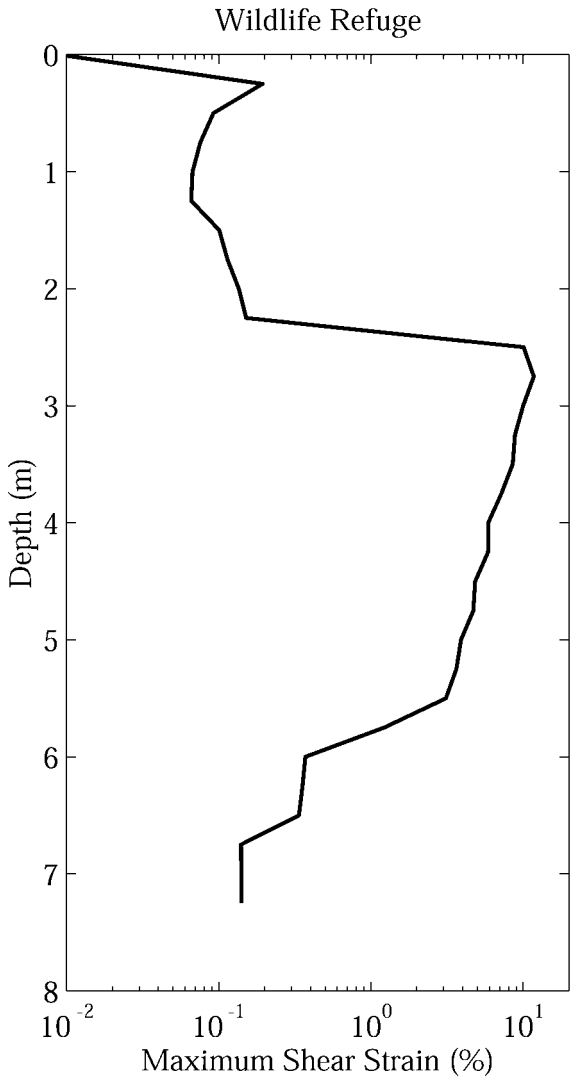

Figure 22. Distribution of maximum shear strain versus depth at the Wildlife Refuge site. Note the large deformations between 2.5- and 5.5-m depth.

Kamae, K., K. Irikura, and A. Pitarka (1998). A technique for simulating strong ground motion using hybrid Green's functions, *Bull. Seism. Soc. Am.* **88,** 357–367.

Kausel, E., and D. Assimaki (2002). Seismic simulation of inelastic soils via frequency-dependent moduli and damping, *J. Eng. Mech.* **128,** 34–45.

Konder, R. L., and J. S. Zelasko (1963). A hyperbolic stress-strain formulation for sands, in *Proc. of 2nd Pan American Conference on Soil Mechanics and Foundation Engineering*, Brazil, 289–324.

Kramer, S. L. (1996). *Geothechnical Earthquake Engineering*, Prentice Hall, New Jersey, 653 pp.

Lee, K. W., and W. D. L. Finn (1978). *DESRA-2: Dynamic Effective Stress Response Analysis of Soil Deposit with Energy Transmitting Boundary Including Assessment of Liquefaction Potential*, Soil Mechanics Series, University of British Columbia, Vancouver.

Masing, G. (1926). Eigenspannungen und Verfertigung beim Messing, in *Proceedings of the 2nd International Congress on Applied Mechanics*, Zurich, Switzerland, 332–335.

Matasovic, J., and M. Vucetic (1993). Analysis of seismic records obtained on November 24, 1987 at the Wildlife Liquefaction Array, Research Report, Civil Engineering Department, University of California, Los Angeles, 94 pp.

Ni, S. H., R. V. Siddharthan, and J. G. Anderson (1997). Characteristics of nonlinear soil response of deep saturated soil deposits, *Bull. Seism. Soc. Am.* **87,** 342–355.

O'Connell, D. R. H. (1999). Replication of apparent nonlinear seismic response with linear wave propagation models, *Science* **283,** 2045–2033.

Porcella, R. L. (1980). Atypical accelerograms recorded during recent earthquakes, Seismic Engineering Program Report, May–August 1980, Geological Survey Circular 854-B, 1–7.

Prevost, J. H., and C. M. Keane (1990). Shear stress-strain curve generation from simple material parameters, *J. Geotech. Eng.* **116,** 1255–1263.

Prevost, J. H., and R. Popescu (1996). Constitutive relations for soil materials, *Electronic J. Geotech. Eng.*

Pyke, R. (1979). Nonlinear soil model for irregular cyclic loadings. *J. Geotech. Eng. Div.* **105,** 715–726.

Ramsamooj, D. V., and A. J. Alwash (1997). Model prediction of cyclic response of soil, *J. Geotech. Eng. ASCE* **116,** 1053–1072.

Satoh, T., M. Horike, Y. Takeuchi, T. Uetake, and H. Suzuki (1997). Nonlinear behavior of scoria soil sediments evaluated from borehole records in Eastern Shizuoka Prefecture, Japan, *Earthquake Eng. Struct. Dyn.* **26,** 781–795.

Satoh, T., T. Sato, and H. Kawase (1995). Nonlinear behavior of soil sediments identified by using borehole records observed at the Ashigara Valley, Japan, *Bull. Seism. Soc. Am.* **85,** 1821–1834.

Schnabel, P. B., H. B. Seed, and J. Lysmer (1972). Modification of seismogram records for effects of local soil conditions, *Bull. Seism. Soc. Am.* **62,** 1649–1664.

Seed, H. B., and I. M. Idriss (1970). Analyses of ground motions at Union Bay, Seattle during earthquakes and distant nuclear blasts, *Bull. Seism. Soc. Am.* **60,** 125–136.

Steidl, J. H., A. G. Tumarkin, and R. J. Archuleta (1996). What is a reference site? *Bull. Seism. Soc. Am.* **86,** 1733–1748.

Towhata, I., and K. Ishihara (1985). Modeling soil behavior under principal axes rotation, paper presented at the Fifth International Conference on Numerical Methods in Geomechanics, Nagoya, Japan 523–530.

Vucetic, M. (1990). Normalized behavior of clay under irregular cylic loading, *Can. Geotech. J.* **27,** 29–46.

Vucetic, M., and V. Thilakaratne (1989). Liquefaction at the Wildlife Site—effect of soil stiffness on seismic response, paper presented at the *Fourth International Conference on Soil Dynamics and Earthquake Engineering*, Mexico, 37–52.

Wen, K., I. Beresnev, and Y. T. Yeh (1994). Nonlinear soil amplification inferred from downhole strong seismic motion data, *Geophys. Res. Lett.* **21,** 2625–2628.

Youd, T. L., and T. L. Holzer (1994). Piezometer performance at the wildlife liquefaction site, California, *J. Geotech. Eng.* **120,** no. 6, 975–995.

Yu, G., J. G. Anderson, and R. V. Siddharthan (1992). On the characteristics of nonlinear soil response, *Bull. Seism. Soc. Am.* **83,** 218–244.

Zeghal, M., and A. W. Elgamal (1994). Analysis of site liquefaction using earthquake records, *J. Geotech. Eng.* **120,** no. 6, 996–1017.

Zeghal, M., A. W. Elgamal, and E. Parra (1996). Analyses of site liquefaction using downhole array seismic records, paper presented at the 11th World Conference on Earthquake Engineering, paper 371, 23–28 June 1996, Acapulco, Mexico.

Zienkiewicz, O. C., K. H. Leung, E. Hinton, and C. T. Chang (1982). Liquefaction and permanent deformation under dynamic conditions—numerical solution and constitutive relations, in *Soil Mechanics—Transient and Cyclic Loads*, G. N. Pande and and O. C. Zienkiewicz (Editor) 71–104.

Bureau d'Evaluation du Risque Sismique et de Sûreté des Installations
Institut de Radioprotection et de Sûreté Nucléaire
BP 17, Fontenay-aux-Roses, Cedex, France
fabian.bonilla@irsn.fr
(L.F.B.)

Institute for Crustal Studies
1140 Girvetz Hall University of California
Santa Barbara, California 93106
ralph@crustal.ucsb.edu
(R.J.A.)

Institute for Crustal Studies
1140 Girvetz Hall University of California
Santa Barbara, California 93106
daniel@crustal.ucsb.edu
(R.J.A., D.L.)

Manuscript received 23 June 2004.